A curved 2.5D model for simulating dynamic responses of coupled track-tunnel-soil system in curved section due to moving loads

Longxiang Ma[a,*], Huajiang Ouyang[b], Chang Sun[a], Ruitong Zhao[a], Le Wang[c]

[a] MOE Key Laboratory of Transportation Tunnel Engineering, Southwest Jiaotong University, Chengdu 610031, China;

[b] School of Engineering, University of Liverpool, Liverpool L69 3GH, UK;

[c] China Design Group Co., LTD., Nanjing 210014, China

Abstract: Ground-borne vibration excited by railway traffic has attracted much research in very recent years and its conventional three-dimensional numerical analysis is known to be tedious and time consuming. Advanced numerical models based on a significant model reduction which can simulate this problem in an efficient way have been developed only for straight railway lines. To achieve a significant reduction of the number of degrees-of-freedom in the determination of dynamic responses of a coupled curved track-tunnel-soil system due to moving loads, a curved two-and-a-half-dimensional (2.5D) model is presented in this paper. In this model, the track-tunnel-soil system is assumed to be invariant in the longitudinal direction. Further, a curved 2.5D finite element method is proposed to model the tunnel-soil system and provide an appropriate artificial boundary of the computation domain, while a 2.5D analytical method considering the longitudinal, transverse, vertical and rotational motions of the rail is developed to model the curved track. By exploiting the force equilibrium and displacement compatibility conditions, the curved track with an analytical solution is coupled to the curved tunnel-soil system with a finite element solution, leading to the governing equation of motion of the whole curved track-tunnel-soil system. Through comparisons with other theoretical models, the proposed model is validated. Numerical examples show that the proposed model can efficiently simulate the dynamic responses of the curved track-tunnel-soil system due to its significant advantage that the discretization and solution are required over only the cross section. Some interesting dynamic phenomena of the curved track-tunnel-soil system subjected to generalized moving loads acting on the rail are also found through the numerical analyses.

Keywords: numerical simulation; ground-borne vibration; 2.5D modelling approach; coupled track-tunnel-soil system; curved section; moving load problem.

1. Introduction

Traffic-induced ground-borne vibrations, especially those induced by metro traffic, may have negative influences on the normal life of the residents, the operations of delicate instruments, and the historical buildings along the traffic infrastructures [1–3]. Thus they have become a major concern in urban areas around the world. To better understand these vibrations, simulating and analysing the vibration responses of the coupled traffic infrastructure and soil system due to dynamic loads produced by various modes of transportation are needed.

Great efforts have been made in quantifying the ground-borne vibrations due to various dynamic

---

*Corresponding author.

E-mail address: malongxiang@home.swjtu.edu.cn (L.X. Ma).

Nomenclature

Roman symbols

a	distance between the rail centroid and the rail bottom
b	half width of the rail bottom
$\mathbf{B}$	strain matrix in the FEM
c_j , $c_j^{'}$	damping quantities
C_P	P-wave speed of the soil
C_S	S-wave speed of the soil
$\mathbf{C}_{\text{boundary}}^{e}$	damping matrix of an artificial boundary element
$\mathbf{C}^g$	global damping matrix of the whole FE model
d_b	distance between the excitation source and the artificial boundary
$\mathbf{D}$	constitutive matrix of the viscoelastic medium
E , E_m	Young's moduli
f	external force of the viscoelastic medium modelled by FEM
f_0	load's frequency
f_{ij} , f_{ijp}	reaction forces of the tunnel base to the rails
$\mathbf{f}$, $\mathbf{f}_j$	external force vector of the viscoelastic medium modelled by FEM
F_{ij}	external force applied on the track
$\mathbf{F}$	external force vector applied on the track
$\mathbf{F}^e$	equivalent nodal force vector of a finite element
$\mathbf{F}^g$	equivalent nodal force vector of the whole FE model
G , G_m	shear moduli
i	unit imaginary number
I_d	torsional constant of the rail
I_0	rail's polar moment of area about the centroid of the cross-section
I_Y	rail's second moment of area with respect to Y axis
I_Z	rail's second moment of area with respect to Z axis
$\mathbf{J}$	FEM Jacobian matrix
k	wavenumber in the θ direction
k_j , $k_j^{'}$	stiffness quantities
$\mathbf{K}^e$, $\mathbf{K}_{ij}^e$	stiffness matrices of a four-node curved 2.5D finite element
$\mathbf{K}_{\text{boundary}}^{e}$	stiffness matrix of an artificial boundary element
$\mathbf{K}^g$	global stiffness matrix of the whole FE model
$\mathbf{K}_{ij}^g$	global stiffness matrix corresponding to $\mathbf{K}_{ij}^e$
$\mathbf{K}_{\text{boudary}}^{g}$	global stiffness matrix of the whole artificial boundary
$\mathbf{L}$	differential operation matrix of the strain-displacement relation
m	mass per unit length of the rail

$M_{i\varphi}$	external moment applied to the rail
$\mathbf{M}^e$	mass matrix of a finite element
$\mathbf{M}^g$	global mass matrix of the whole FE model
$\mathbf{N}$	FEM shape function
P_{Li}, P_{Lij}	time-domain magnitudes of the external force acting on the left rail
R	radius of the curved tunnel
R_i	radius of the left rail (i=L) or the right rail (i=R)
u_{ij}	displacement of the rail
u_{pj}^b, u_{pji}^b	displacement quantities of the tunnel base points
$\mathbf{u}$	displacement vector of the viscoelastic medium modelled by FEM
$\mathbf{U}^e$	nodal displacement vector of a finite element
$\mathbf{U}^g$	nodal displacement vector of the whole FE model
$\mathbf{U}^t$	displacement vector of the track
v	linear velocity of the moving load
v_θ	angular velocity of the moving load
Greek symbols	
α	superelevation angle of the curved track
α_N, α_T	modified coefficients for the stiffnesses of the artificial boundary
$\mathbf{\Gamma}$	inverse matrix of FEM Jacobian matrix $\mathbf{J}$
$\boldsymbol{\varepsilon}$	strain tensor
ζ	local coordinate of the curved 2.5D finite element
η	local coordinate of the curved 2.5D finite element
λ_m	Lamé coefficient
μ_m	Lamé coefficient
ν_m	Poisson's ratio
ξ, ξ_m	damping ratios
ρ, ρ_m	mass densities
$\boldsymbol{\sigma}$	stress tensor
φ_i	rotational displacement of the rail
ω	circular frequency
Other symbols	
$\tilde{}$	variable in the wavenumber domain
$\hat{}$	variable in the frequency domain
$\tilde{\hat{}}$	variable in the wavenumber-frequency domain
$\bar{}$	amplitude of a harmonic variable

loads representing both the excitation of railway traffic (including metro traffic) and that of roadway traffic in the past decades. For the dynamic responses of a uniform (visco-) elastic half-space or a multi-layered viscoelastic half-space subjected to various moving or stationary dynamic loads, analytical or semi-analytical solutions have been presented by Eason [4], De Barros and Luco [5], Hung and Yang [6], Kausel [7] and Cao et al. [8], respectively. Their outstanding works provided a good understanding of the concerned problem, but when more complicated problems are considered, these analytical or semi-analytical methods are not applicable. In such circumstances, numerical simulation methods are usually needed. Various numerical two-dimensional (2D) and three-dimensional (3D) models based on different methods [9–12] have been developed to determine these ground-borne vibrations, but these conventional numerical models still have some drawbacks. Specifically, the 2D models cannot account for wave propagation in the longitudinal direction of the traffic infrastructure and will underestimate radiation damping of the soil, while the 3D models are inefficient from a computational point of view [13].

A sensible approach to quantify these ground-borne vibrations is to develop advanced numerical models which can overcome the drawbacks of the conventional ones. As a result, there have been two kinds of advanced numerical models proposed by several authors. The first kind is the two-and-a-half-dimensional (2.5D) model, in which the geometry of a system in the longitudinal direction is assumed to be invariant and the solution is required over only the cross section. Various 2.5D models have been developed in recent years, including the coupled finite element-infinite element (FE-IE) model [14,15], the coupled finite element-boundary element (FE-BE) model [16,17], the model based on the coupled integral transformation method and finite element method (ITM-FEM) [18,19], the Pipe-in-Pipe (PiP) model [20–22], the FE model with viscoelastic artificial boundary [23] and the coupled finite element and perfectly matched layer (FEM-PML) model [24–26]. The second kind of advanced models is the periodic model, in which the geometry of the system in the longitudinal direction is assumed to be periodic and a periodic solution is sought. The coupled periodic finite element-boundary element (FE-BE) model [27,28] is the main representative of this kind of models. Both kinds of advanced models can bring a significant reduction of the number of degrees-of-freedom (DoFs) in the simulation of the problem, hence saving a large amount of computational workload. Although there are many advanced models for the ground-borne vibrations induced by moving train or other dynamic loads, to the authors' best knowledge, these models are limited to only straight railway lines or loads moving in straight lines.

When metro traffic is concerned, it can be found that there are plenty of curved metro sections in reality due to the existing layout of a city and other restrictions. Taking the metro network of Beijing as an example, the mileage of curved sections takes up nearly 30% of its total mileage in 2012 [29]. In this circumstance, some buildings which are sensitive to the environmental vibration are inevitably affected by these curved metro sections. For instance, it was reported in 2017 that a laboratory with a number of delicate instruments in Peking University was affected by a curved section of Beijing metro line 16 [30]. When the train negotiates a curved track, much higher complexity occurs in the train-track contact relation and interaction, generating significant asymmetry of loads acting on the internal and external rails [31], non-ignorable lateral wheel-rail loads [32] and even short pitch rail corrugation [33]. These factors, together with the peculiar moving trajectory of a train (or wheel-rail loads) and peculiar structural characteristics of the curved track and tunnel (e.g. the declining tunnel base constructed to satisfy the requirement on the track superelevation), make the ground vibration of a curved metro section quite different from that of a straight one. Specifically, the train-induced ground vibrations of a curved metro section (for those ground points on the inner side of the radius of the curved metro line) were found to be usually greater than those of a straight section with similar conditions, and their radial components were also found to be much greater than their vertical components in a wide region of the ground surface [29]. It is worth noting that the aforementioned understandings on ground vibrations of a curved metro section are mainly obtained through the analyses of field measurement data, and further theoretical studies are still needed for a comprehensive clarification of the specific dynamic features of a curved metro section.

There have been a large number of models reported for dynamic behaviours of curved beams and curved tracks subjected to various dynamic excitations, varying from non-moving or moving harmonic loads to moving train loads. The corresponding literature review can be found in Refs. [34] and [35]. However, numerical studies of the ground-borne vibration of a curved metro section are very limited, which is mainly due to the higher complexity when ground dynamic behaviour is considered. As far as the simulation method of ground-borne vibration of a curved metro section is concerned, it seems that there does not exist a very efficient approach for dealing with this problem as mentioned above and only computation-expensive 3D FE method (such as the work in [30]) is available.

Compared with the simulation of the ground-borne vibration of a straight metro section where only the out-of-plane behaviour of the track is generally considered, both the out-of-plane and in-plane dynamic behaviours of the track should be taken into consideration in the simulation of the ground-borne vibration of a curved metro section due to the much more complex loading condition on the curved track. As a direct result, the ground vibration characteristics under dynamic loads acting on the rail in its transverse and even rotational directions, which have not been given enough attention in the studies of the ground-borne vibration of a straight metro section, become important for a better understanding of the ground-borne vibration of a curved metro section. On the other hand, the effects of the curvature of the track-tunnel system and the track superelevation on the ground vibrations have not been studied yet, also leading to poor understandings on the ground-borne vibration of a curved metro section.

Generally speaking, a completely coupled train-track-tunnel-soil model is needed for a comprehensive study of the ground-borne vibration of a curved metro section. However, establishing this kind of model, especially that with high computational efficiency, is an arduous task and needs a great many of intellectual works. This paper only focuses on the efficient simulation of the dynamic responses of a coupled track-tunnel-soil system in a circular curved (in the remainder of this paper, ‘curved’ refers in particular to ‘circular curved’) section due to moving loads, which can facilitate the establishment of the completely coupled train-track-tunnel-soil model of a curved metro section. Specifically, this paper creates a curved 2.5D model which has high computational efficiency to account for this dynamic problem. In this model, by assuming the geometry of the track-tunnel-soil system in the longitudinal direction to be invariant, a curved 2.5D finite element approach is developed to account for the motion of the tunnel-soil system, while a curved 2.5D analytical approach is developed to account for both the out-of-plane and in-plane motions of the curved track. By introducing the force equilibrium equations and the displacement compatibility equations, the track is coupled to the tunnel-soil system and the governing equation of motion for the whole system is obtained. For deterministic external loads, this model can simulate the response of the coupled curved track-tunnel-soil system in an efficient way, because the discretization and solution are required over only the cross section of the system, thus having the same advantage as the conventional 2.5D models for the straight railway lines or loads moving in straight lines. Based on this model, the effects of the curvature of the track-tunnel system and the track superelevation on the ground vibrations due to moving harmonic loads are discussed, and the ground vibration characteristics under dynamic loads acting on the rail in its different directions are also studied.

In the remainder of this paper, the formulation of the curved 2.5D model for simulating the dynamic responses of the coupled curved track-tunnel-soil system is elaborated in section 2, in which the 2.5D finite element model accounting for the curved tunnel-soil system, the motion of the curved track, the coupling of the track and the tunnel-soil system, the expressions of external loads and the solution of the whole system are discussed. After the validations of the proposed model presented in section 3, some numerical examples demonstrating some particular dynamic characteristics of the coupled curved track-tunnel-soil system under harmonic moving loads are given in section 4. Finally, the conclusions of the present study are summarized in section 5.

2. Formulation of 2.5D model accounting for coupled curved track-tunnel-soil system

2.1 Overall description of the model and basic definitions

When the dynamic responses of a curved track-tunnel-soil system due to moving loads are considered, using the conventional three-dimensional models to simulate it incurs a huge computational workload. Under the motivation of the computational efficiency, a curved 2.5D model accounting for the coupled curved track-tunnel-soil system as shown in Fig. 1 is established in a cylindrical coordinate system by following the idea similar to the conventional 2.5D model accounting for moving load problems of prismatic structures. In this model, the fixed track where the rails are laid on rail pads on concrete sleepers being cast into the tunnel invert is considered, thus the sleepers are included as part of the concrete invert. The discrete distribution of the rail pads is neglected, and the track-tunnel-soil system is assumed to be invariant in the longitudinal direction (θ direction). The tunnel and soil mediums are modelled by the four-node curved 2.5D finite elements. The rails are modelled as two curved Euler beams considering the vertical, transverse, longitudinal and rotational motions, and a 2.5D analytical method is adopted here to account for these motions. The rail pads are modelled as continuously distributed spring-damper elements, which transmit the forces generated by all the motions of the rails to the tunnel-soil system. Besides, in order to truncate the infinite domain into a finite computation domain and provide an appropriate computation boundary, the curved 2.5D consistent viscoelastic boundary elements are also introduced to represent the artificial boundaries of the computation domain in the present model.

In the current work, the dynamic responses of the curved track-tunnel-soil system due to point loads moving in the longitudinal direction (θ direction) are the focus. Since the vertical and transverse (relative to the rail) loads acting on the rail head are the main loads generated by the train moving on the curved track in the reality, the external loads acting in the vertical and transverse directions of the rail and the external rotational moments originating from the aforementioned two kinds of loads due to the fact that their action lines do not, or at least do not always, pass through the centroid of the rail are considered in the present model. Besides, these loads considered herein are assumed to never stop moving, which means that the loads are always moving in circle. However, when the loads complete a circle and return at particular points, their positions in the θ direction are considered to increase by 2π on the basis of the original coordinates. Thus, the limit of the θ coordinate of the curved track-tunnel-soil system is considered to be from $-\infty$ to $+\infty$ and the external loads are assumed to move from $\theta = -\infty$ to $\theta = +\infty$ in the present model. Obviously, this treatment is very appropriate and will not affect the simulation accuracy due to the relatively large radius of the railway infrastructure and the fact that the external loads will not return to a particular θ in the reality. More importantly, this treatment makes the Fourier transform in the longitudinal direction applicable, which will be very helpful for reducing the dimensionality of the problem and establishing the curved 2.5D model.

As the Fourier transforms with respect to space coordinate θ and time t and their corresponding inverse transforms are required for the establishment of the curved 2.5D model, their definitions in the present paper are first given. The Fourier transform with respect to space coordinate θ, which transforms a variable concerned in the space domain to that in the wavenumber domain, and its corresponding inverse transform are defined as

$$\tilde{u}(k) = \int_{-\infty}^{+\infty} u(\theta) \mathrm{e}^{\mathrm{i}k\theta} \mathrm{d}\theta \tag{1a}$$

$$u(\theta) = \frac{1}{2\pi} \int_{-\infty}^{+\infty} \tilde{u}(k) \mathrm{e}^{-\mathrm{i}k\theta} \mathrm{d}k \tag{1b}$$

where i is the unit imaginary number, and k is the wavenumber in the θ direction, which is a dimensionless quantity here. The tilde "~" above a variable denotes its representation in the wavenumber domain.

Simultaneously, the Fourier transform with respect to time *t* which transforms the variable in the time domain to that in the frequency domain and its corresponding inverse transform in the present paper are defined as

$$\hat{u}(\omega)=\int_{-\infty}^{+\infty}u(t)\mathrm{e}^{-\mathrm{i}\omega t}\mathrm{d}t \tag{2a}$$

$$u(t)=\frac{1}{2\pi}\int_{-\infty}^{+\infty}\hat{u}(\omega)\mathrm{e}^{\mathrm{i}\omega t}\mathrm{d}\omega \tag{2b}$$

where ω is the circular frequency. The hat "^" above a variable denotes its representation in the frequency domain.

2.2 Formulation of curved 2.5D FE model for tunnel-soil system

2.2.1 Four-node curved 2.5D finite element accounting for tunnel and soil mediums

In the present model, four-node curved 2.5D finite elements as shown in Fig. 2 are adopted to model the tunnel and soil mediums. Following the usual steps of the finite element method procedure, namely the weak formulation [36], the following frequency-domain equilibrium equation in cylindrical coordinates can be derived for the three-dimensional space domain $\varOmega^e$ represented by this kind of element:

$$\begin{aligned}&\int_{\varOmega^e}[\delta\hat{\boldsymbol{\varepsilon}}(r,\theta,z,\omega)]^T\hat{\boldsymbol{\sigma}}(r,\theta,z,\omega)\,\mathrm{d}\varOmega-\omega^2\int_{\varOmega^e}[\delta\hat{\mathbf{u}}(r,\theta,z,\omega)]^T\rho_m\hat{\mathbf{u}}(r,\theta,z,\omega)\,\mathrm{d}\varOmega\\&=\int_{\varGamma^e}[\delta\hat{\mathbf{u}}(r,\theta,z,\omega)]^T\hat{\mathbf{f}}(r,\theta,z,\omega)\,\mathrm{d}\varGamma\end{aligned} \tag{3}$$

where $\hat{\mathbf{u}}=[\hat{u}_r,\hat{u}_\theta,\hat{u}_z]^T$, $\hat{\boldsymbol{\varepsilon}}=[\hat{\varepsilon}_r,\hat{\varepsilon}_\theta,\hat{\varepsilon}_z,\hat{\gamma}_{\theta z},\hat{\gamma}_{zr},\hat{\gamma}_{r\theta}]^T$ and $\hat{\boldsymbol{\sigma}}=[\hat{\sigma}_r,\hat{\sigma}_\theta,\hat{\sigma}_z,\hat{\sigma}_{\theta z},\hat{\sigma}_{zr},\hat{\sigma}_{r\theta}]^T$ are respectively the displacement, strain and stress vectors in the frequency domain; $\delta\hat{\mathbf{u}}$ and $\delta\hat{\boldsymbol{\varepsilon}}$ denote the virtual displacement and strain vectors, respectively; ρ_m is the density of the medium; $\hat{\mathbf{f}}$ is the external traction acting on the Neumann boundary $\varGamma^e$ of $\varOmega^e$; the superscript *T* denotes the matrix transpose.

Applying the Parseval's theorem [19,37] in the θ direction, Eq. (3) can be further elaborated as follows:

$$\begin{aligned}&\frac{1}{2\pi}\int_{-\infty}^{+\infty}\iint_A[\delta\tilde{\hat{\boldsymbol{\varepsilon}}}(r,-k,z,\omega)]^T\tilde{\hat{\boldsymbol{\sigma}}}(r,k,z,\omega)r\mathrm{d}r\mathrm{d}z\mathrm{d}k\\&-\frac{\omega^2}{2\pi}\int_{-\infty}^{+\infty}\iint_A[\delta\tilde{\hat{\mathbf{u}}}(r,-k,z,\omega)]^T\rho_m\tilde{\hat{\mathbf{u}}}(r,k,z,\omega)r\mathrm{d}r\mathrm{d}z\mathrm{d}k\\&=\frac{1}{2\pi}\int_{-\infty}^{+\infty}\int_s[\delta\tilde{\hat{\mathbf{u}}}(r,-k,z,\omega)]^T\tilde{\hat{\mathbf{f}}}(r,k,z,\omega)r\mathrm{d}s\mathrm{d}k\end{aligned} \tag{4}$$

where *A* and *s* denote the cross section of an element and its circumference over which the area and line integrations in Eq. (4) are defined, respectively. The hat "$\tilde{\wedge}$" above a variable denotes its representation in the wavenumber-frequency domain.

The standard finite element discretization procedure can be adopted in Eq. (4) to derive the discretized equation of equilibrium. Introducing the shape functions of coordinates, the global coordinates of an arbitrary point in the element concerned can be expressed as the interpolation of the global coordinates of its four nodes:

$$r=\sum_{i=1}^{4}N_i r_i \tag{5a}$$

$$z=\sum_{i=1}^{4}N_i z_i \tag{5b}$$

where r_i and z_i are the global coordinates of node *i* ($i=1,2,3,4$) of the element concerned; N_i is the shape function expressed in terms of the two local element coordinates η and ζ, whose detailed expression is as follows:

$$N_i=(1+\eta\eta_i)(1+\zeta\zeta_i)/4 \tag{6}$$

in which η_i and ζ_i are the two local element coordinates of node *i*.

Thus, the Jacobian matrix which transforms the local element coordinates to the global coordinates can be derived as:

$$\mathbf{J}(\eta,\zeta)=\frac{\partial(r,z)}{\partial(\eta,\zeta)}=\begin{bmatrix}\dfrac{\partial N_1}{\partial\eta} & \dfrac{\partial N_2}{\partial\eta} & \dfrac{\partial N_3}{\partial\eta} & \dfrac{\partial N_4}{\partial\eta}\\ \dfrac{\partial N_1}{\partial\zeta} & \dfrac{\partial N_2}{\partial\zeta} & \dfrac{\partial N_3}{\partial\zeta} & \dfrac{\partial N_4}{\partial\zeta}\end{bmatrix}\begin{bmatrix}r_1 & z_1\\ r_2 & z_2\\ r_3 & z_3\\ r_4 & z_4\end{bmatrix} \tag{7}$$

On the other hand, introducing the shape functions shown in Eq. (6) to describe the displacement field of the element concerned, $\tilde{\tilde{\mathbf{u}}}(r,k,z,\omega)$ can be expressed as

$$\tilde{\tilde{\mathbf{u}}}(r,k,z,\omega)=\mathbf{N}(\eta,\zeta)\tilde{\tilde{\mathbf{U}}}^{e}(k,\omega) \tag{8}$$

where $\tilde{\tilde{\mathbf{U}}}^{e}(k,\omega)$ is the nodal displacement vector that collects all the displacements of the four nodes of the element concerned, and $\mathbf{N}(\eta,\zeta)$ is the shape function matrix, which can be expressed as

$$\mathbf{N}(\eta,\zeta)=\begin{bmatrix}N_1 & 0 & 0 & N_2 & 0 & 0 & N_3 & 0 & 0 & N_4 & 0 & 0\\ 0 & N_1 & 0 & 0 & N_2 & 0 & 0 & N_3 & 0 & 0 & N_4 & 0\\ 0 & 0 & N_1 & 0 & 0 & N_2 & 0 & 0 & N_3 & 0 & 0 & N_4\end{bmatrix} \tag{9}$$

The strain-displacement relations in the wavenumber-frequency domain can be derived by applying the two forward Fourier transforms predefined in Eq. (1) to the conventional ones in the space-time domain, given as:

$$\tilde{\tilde{\boldsymbol{\varepsilon}}}(r,k,z,\omega)=\mathbf{L}(r,k,z)\tilde{\tilde{\mathbf{u}}}(r,k,z,\omega) \tag{10}$$

where $\mathbf{L}(r,k,z)$ is the differential operation matrix, whose detailed expression is given below:

$$\mathbf{L}(r,k,z)=\begin{bmatrix}\partial/\partial r & 1/r & 0 & 0 & \partial/\partial z & -\mathrm{i}k/r\\ 0 & -\mathrm{i}k/r & 0 & \partial/\partial z & 0 & \partial/\partial r-1/r\\ 0 & 0 & \partial/\partial z & -\mathrm{i}k/r & \partial/\partial r & 0\end{bmatrix}^{T} \tag{11}$$

Substituting Eq. (8) into Eq. (10), the strain vector $\tilde{\tilde{\boldsymbol{\varepsilon}}}(r,k,z,\omega)$ can be elaborated in terms of the nodal displacement vector $\tilde{\tilde{\mathbf{U}}}^{e}(k,\omega)$:

$$\tilde{\tilde{\boldsymbol{\varepsilon}}}(r,k,z,\omega)=\mathbf{B}(\eta,k,\zeta)\tilde{\tilde{\mathbf{U}}}^{e}(k,\omega) \tag{12}$$

where $\mathbf{B}(\eta,k,\zeta)=\mathbf{L}(r,k,z)\mathbf{N}(\eta,\zeta)$ is the strain matrix, which can be further expressed in the following form through some mathematical manipulations:

$$\mathbf{B}(\eta,k,\zeta)=(\mathbf{H}_1+\mathrm{i}k\mathbf{H}_2)\mathbf{R} \tag{13}$$

in which

$$\mathbf{H}_1=\begin{bmatrix} \Gamma_{11} & \Gamma_{12} & 0 & 0 & 0 & 0 & 0 & 0 & 0 \\ 0 & 0 & 1/(2r) & 0 & 0 & 1/(2r) & 0 & 0 & -1/(2r) \\ 0 & 0 & 0 & \Gamma_{21} & \Gamma_{22} & 0 & 0 & 0 & 0 \\ 0 & 0 & 0 & 0 & 0 & 0 & \Gamma_{21} & \Gamma_{22} & 0 \\ \Gamma_{21} & \Gamma_{22} & 0 & \Gamma_{11} & \Gamma_{12} & 0 & 0 & 0 & 0 \\ 0 & 0 & -1/(2r) & 0 & 0 & 1/(2r) & \Gamma_{11} & \Gamma_{12} & -1/(2r) \end{bmatrix}, \tag{14}$$

$$\mathbf{H}_2=\frac{1}{2r}\times\begin{bmatrix} 0 & 0 & 0 & 0 & 0 & 0 & 0 & 0 & 0 \\ 0 & 0 & -1 & 0 & 0 & 1 & 0 & 0 & -1 \\ 0 & 0 & 0 & 0 & 0 & 0 & 0 & 0 & 0 \\ 0 & 0 & 1 & 0 & 0 & -1 & 0 & 0 & -1 \\ 0 & 0 & 0 & 0 & 0 & 0 & 0 & 0 & 0 \\ 0 & 0 & -1 & 0 & 0 & -1 & 0 & 0 & 1 \end{bmatrix}, \tag{15}$$

$$\mathbf{R}=[\mathbf{R}_1,\mathbf{R}_2,\mathbf{R}_3,\mathbf{R}_4], \tag{16}$$

with Γ_{ij} being the corresponding element in matrix $\mathbf{\Gamma}$ that satisfies the relation $\mathbf{\Gamma}=\mathbf{J}^{-1}$, and

$$\mathbf{R}_i=\begin{bmatrix} \partial N_i/\partial\eta & \partial N_i/\partial\zeta & N_i & 0 & 0 & N_i & 0 & 0 & 0 \\ 0 & 0 & N_i & 0 & 0 & 0 & \partial N_i/\partial\eta & \partial N_i/\partial\zeta & N_i \\ 0 & 0 & 0 & \partial N_i/\partial\eta & \partial N_i/\partial\zeta & N_i & 0 & 0 & N_i \end{bmatrix}^T. \tag{17}$$

The stress vector $\tilde{\hat{\boldsymbol{\sigma}}}(r,k,z,\omega)$ can be related to the strain vector $\tilde{\hat{\boldsymbol{\varepsilon}}}(r,k,z,\omega)$ through the constitutive relation, resulting in:

$$\tilde{\hat{\boldsymbol{\sigma}}}(r,k,z,\omega)=\mathbf{D}\mathbf{B}(\eta,k,\zeta)\tilde{\hat{\mathbf{U}}}^e(k,\omega) \tag{18}$$

where $\mathbf{D}$ is the constitutive matrix, whose detailed expression can be found elsewhere [36]. It should be emphasized that the material damping of the medium can be taken into account through use of the complex Lamé coefficients, i.e. $\lambda_m^*=\lambda_m[1+2\mathrm{i}\xi_m\,\mathrm{sgn}(\omega)]$ and $\mu_m^*=\mu_m[1+2\mathrm{i}\xi_m\,\mathrm{sgn}(\omega)]$ with ξ_m being the damping ratio of the medium, in the expression of $\mathbf{D}$.

Substituting Eq. (8), Eq. (12) and Eq. (18) into Eq. (4) and taking the fact into consideration that the virtual displacement field $\delta\tilde{\hat{\mathbf{U}}}^e(-k,\omega)$ is arbitrary and non-zero, yields the discretized equation of equilibrium of the four-node 2.5D element concerned:

$$\mathbf{K}^e(k)\tilde{\hat{\mathbf{U}}}^e(k,\omega)-\omega^2\mathbf{M}^e\tilde{\hat{\mathbf{U}}}^e(k,\omega)=\tilde{\hat{\mathbf{F}}}^e(k,\omega) \tag{19}$$

where the stiffness matrix $\mathbf{K}^e(k)$ and the mass matrix $\mathbf{M}^e$ can be respectively written as

$$\mathbf{K}^e(k)=\int_{-1}^{1}\int_{-1}^{1}\mathbf{B}^T(\eta,-k,\zeta)\mathbf{D}\mathbf{B}(\eta,k,\zeta)r(\eta,\zeta)\,|\,\mathbf{J}(\eta,\zeta)\,|\mathrm{d}\eta\mathrm{d}\zeta, \tag{20}$$

$$\mathbf{M}^e=\int_{-1}^{1}\int_{-1}^{1}\rho_m\mathbf{N}^T(\eta,\zeta)\mathbf{N}(\eta,\zeta)r(\eta,\zeta)\,|\,\mathbf{J}(\eta,\zeta)\,|\,\mathrm{d}\eta\mathrm{d}\zeta. \tag{21}$$

$\tilde{\hat{\mathbf{F}}}^e(k,\omega)$ is the equivalent nodal force vector, which can be split into two parts in the present model: one part, denoted as $\tilde{\hat{\mathbf{F}}}_1^e(k,\omega)$, is generated by the internal stresses between the interfaces of the element concerned and its neighbouring finite elements, and the other part, denoted as $\tilde{\hat{\mathbf{F}}}_2^e(k,\omega)$, is related to the external loads of the tunnel-soil system modelled by curved 2.5D finite elements. Obviously, $\tilde{\hat{\mathbf{F}}}_1^e(k,\omega)$ will be equilibrated by the equal and opposite nodal forces acting on the neighbouring 2.5D finite elements, which will then cancel each other during the assembly of the system equation. Thus only $\tilde{\hat{\mathbf{F}}}_2^e(k,\omega)$ needs to be considered here. The expression of $\tilde{\hat{\mathbf{F}}}_2^e(k,\omega)$ is given as follows:

$$\tilde{\hat{\mathbf{F}}}_2^e(k,\omega)=\sum_j \mathbf{N}^T(\eta_j,\zeta_j)\tilde{\hat{\mathbf{f}}}_j(k,\omega)r(\eta_j,\zeta_j) \tag{22}$$

in which $\tilde{\hat{\mathbf{f}}}_j(k,\omega)$ is the external load of the element concerned that is transmitted from the curved rail. Obviously, only for the element relating to the rails, $\tilde{\hat{\mathbf{f}}}_j(k,\omega)$ has a non-zero value.

Substituting Eq. (13) into Eq. (20), $\mathbf{K}^e(k)$ can be further expressed as a linear combination of four sub-matrices which are totally independent of wavenumber *k*:

$$\mathbf{K}^e(k)=\mathbf{K}_{11}^e+\mathrm{i}k\mathbf{K}_{12}^e-\mathrm{i}k\mathbf{K}_{21}^e+k^2\mathbf{K}_{22}^e \tag{23}$$

where

$$\mathbf{K}_{11}^e=\int_{-1}^{1}\int_{-1}^{1}\mathbf{R}^T\mathbf{H}_1^T\mathbf{D}\mathbf{H}_1\mathbf{R}r\,|\,\mathbf{J}\,|\mathrm{d}\eta\mathrm{d}\zeta\,, \tag{24a}$$

$$\mathbf{K}_{12}^e=\int_{-1}^{1}\int_{-1}^{1}\mathbf{R}^T\mathbf{H}_1^T\mathbf{D}\mathbf{H}_2\mathbf{R}r\,|\,\mathbf{J}\,|\mathrm{d}\eta\mathrm{d}\zeta\,, \tag{24b}$$

$$\mathbf{K}_{21}^e=[\mathbf{K}_{12}^e]^T=\int_{-1}^{1}\int_{-1}^{1}\mathbf{R}^T\mathbf{H}_2^T\mathbf{D}\mathbf{H}_1\mathbf{R}r\,|\,\mathbf{J}\,|\mathrm{d}\eta\mathrm{d}\zeta\,, \tag{24c}$$

$$\mathbf{K}_{22}^e=\int_{-1}^{1}\int_{-1}^{1}\mathbf{R}^T\mathbf{H}_2^T\mathbf{D}\mathbf{H}_2\mathbf{R}r\,|\,\mathbf{J}\,|\mathrm{d}\eta\mathrm{d}\zeta\,. \tag{24d}$$

Apparently, with the help of Eq. (23), the numerical performance of the computations of the stiffness matrices $\mathbf{K}^e(k)$ with different values of *k* can be significantly improved.

Since all the above integrals relating to the discretized equation of equilibrium have been expressed in terms of the two local coordinates η and ζ, they can be easily computed using the 2D Gaussian quadrature [36].

2.2.2 2.5D consistent viscoelastic artificial boundary element

When an infinite domain whose dynamic response needs to be solved is represented by a finite domain, a virtual artificial boundary condition should be introduced to avoid the significant wave reflection at the computation boundary. Here, the verified consistent viscoelastic artificial boundary proposed by Liu et al. [38] is adopted. However, this artificial boundary is applicable to only a 3D problem. So it is further developed in the present paper to make it applicable to the present curved 2.5D problem.

The lateral and bottom boundaries of the present model can be artificially set to be perpendicular or parallel to the ground surface that is assumed to be horizontal, as shown in Fig. 3. The frequency-domain governing equation of motion of a bottom artificial boundary element shown in Fig. 4 can be written as

$$\mathbf{K}_b\hat{\mathbf{u}}(s,\theta,\omega)+\mathrm{i}\omega\mathbf{C}_b\hat{\mathbf{u}}(s,\theta,\omega)=\hat{\mathbf{f}}(s,\theta,\omega) \tag{25}$$

where $\hat{\mathbf{u}}(s,\theta,\omega)$ and $\hat{\mathbf{f}}(s,\theta,\omega)$ are the displacement and external load vectors, respectively; s is the global coordinate along the element concerned; $\mathbf{K}_b$ and $\mathbf{C}_b$ are respectively the corresponding stiffness and damping matrices, which can be written as

$$\mathbf{K}_b = \begin{bmatrix} k_T & 0 & 0 \\ 0 & k_T & 0 \\ 0 & 0 & k_N \end{bmatrix} \tag{26}$$

$$\mathbf{C}_b = \begin{bmatrix} c_T & 0 & 0 \\ 0 & c_T & 0 \\ 0 & 0 & c_N \end{bmatrix} \tag{27}$$

in which k_N and k_T are respectively the normal and tangential stiffnesses of the artificial boundary, while c_N and c_T are respectively the normal and tangential dampings of the artificial boundary. They can be computed through the following equations according to Ref. [38]:

$$k_N = \alpha_N G_s / d_b\,,\ \ k_T = \alpha_T G_s / d_b \tag{28}$$

$$c_N = \rho_s C_P\,,\ \ c_T = \rho_s C_S \tag{29}$$

where α_N and α_T are respectively the modified coefficients for the stiffnesses in the normal and tangential directions, whose recommended values 1.33 and 0.67 are used in the present paper; G_s, ρ_s, C_P and C_S are the shear modulus, density, P-wave speed and S-wave speed of the corresponding soil medium in which the artificial boundary element concerned locates, respectively; d_b is the distance between the excitation source and the boundary, which takes the approximate value of the perpendicular distance from the middle point of tunnel base to the boundary in the present paper.

To derive the stiffness and damping matrices of this element, Eq. (25) is cast in a weak form by considering a virtual displacement field $\delta\hat{\mathbf{u}}(s,\theta,\omega)$:

$$\int_{\Gamma^e} [\delta\hat{\mathbf{u}}(s,\theta,\omega)]^T (\mathbf{K}_b \hat{\mathbf{u}}(s,\theta,\omega) + \mathrm{i}\omega \mathbf{C}_b \hat{\mathbf{u}}(s,\theta,\omega))\,\mathrm{d}\Gamma = \int_{\Gamma^e} [\delta\hat{\mathbf{u}}(s,\theta,\omega)]^T \hat{\mathbf{f}}(s,\theta,\omega)\,\mathrm{d}\Gamma \tag{30}$$

where Γ^e is the actual boundary area in the 3D space represented by the element concerned.

Similar to the above derivation, Eq. (30) can be further shown to be using the Parseval's theorem:

$$\begin{aligned} &\frac{1}{2\pi}\int_{-\infty}^{+\infty}\int_s [\delta\tilde{\hat{\mathbf{u}}}(s,-k,\omega)]^T [\mathbf{K}_b \tilde{\hat{\mathbf{u}}}(s,k,\omega) + \mathrm{i}\omega \mathbf{C}_b \tilde{\hat{\mathbf{u}}}(s,k,\omega)] r(s)\,\mathrm{d}s\mathrm{d}k \\ &= \frac{1}{2\pi}\int_{-\infty}^{+\infty}\int_s [\delta\tilde{\hat{\mathbf{u}}}(s,-k,\omega)]^T \tilde{\hat{\mathbf{f}}}(s,k,\omega) r(s)\,\mathrm{d}s\mathrm{d}k \end{aligned} \tag{31}$$

Introducing the shape functions, the displacement field $\tilde{\hat{\mathbf{u}}}(s,k,\omega)$ of the element concerned can be expressed as follows using the corresponding nodal displacement vector $\tilde{\hat{\mathbf{U}}}^e(k,\omega)$:

$$\tilde{\hat{\mathbf{u}}}(s,k,\omega) = \mathbf{N}(\eta)\tilde{\hat{\mathbf{U}}}^e(k,\omega) \tag{32}$$

where η is the local coordinate, and the shape function matrix $\mathbf{N}(\eta)$ can be written as

$$\mathbf{N}(\eta) = \frac{1}{2} \times \begin{bmatrix} 1-\eta & 0 & 0 & 1+\eta & 0 & 0 \\ 0 & 1-\eta & 0 & 0 & 1+\eta & 0 \\ 0 & 0 & 1-\eta & 0 & 0 & 1+\eta \end{bmatrix} \tag{33}$$

Substituting Eq. (32) into Eq. (31) and taking the fact into consideration that the virtual displacement field $\delta\tilde{\hat{\mathbf{U}}}^e(-k,\omega)$ is arbitrary and non-zero, one can finally obtain the equilibrium equation of the element concerned:

$$\mathbf{K}^e_{\text{boundary}}\tilde{\tilde{\mathbf{U}}}^e(k,\omega)+\mathrm{i}\omega\mathbf{C}^e_{\text{boundary}}\tilde{\tilde{\mathbf{U}}}^e(k,\omega)=\tilde{\tilde{\mathbf{F}}}^e(k,\omega) \tag{34}$$

where $\tilde{\tilde{\mathbf{F}}}^e(k,\omega)$ is the equivalent nodal force vector, which will then cancel during the assembly of the system equation and does not need more attention; $\mathbf{K}^e_{\text{boundary}}$ and $\mathbf{C}^e_{\text{boundary}}$ are respectively the stiffness and damping matrices of the element concerned, whose detailed expressions are given below

$$\begin{aligned}\mathbf{K}^e_{\text{boundary}}&=\frac{L}{2}\int_{-1}^{1}\mathbf{N}^T(\eta)\mathbf{K}_b\mathbf{N}(\eta)r(\eta)\mathrm{d}\eta\\&=\frac{L}{12}\times\begin{bmatrix}(3r_1+r_2)k_T & 0 & 0 & (r_1+r_2)k_T & 0 & 0\\ 0 & (3r_1+r_2)k_T & 0 & 0 & (r_1+r_2)k_T & 0\\ 0 & 0 & (3r_1+r_2)k_N & 0 & 0 & (r_1+r_2)k_N\\ (r_1+r_2)k_T & 0 & 0 & (r_1+3r_2)k_T & 0 & 0\\ 0 & (r_1+r_2)k_T & 0 & 0 & (r_1+3r_2)k_T & 0\\ 0 & 0 & (r_1+r_2)k_N & 0 & 0 & (r_1+3r_2)k_N\end{bmatrix}\end{aligned} \tag{35}$$

$$\begin{aligned}\mathbf{C}^e_{\text{boundary}}&=\frac{L}{2}\int_{-1}^{1}\mathbf{N}^T(\eta)\mathbf{C}_b\mathbf{N}(\eta)r(\eta)\mathrm{d}\eta\\&=\frac{L}{12}\times\begin{bmatrix}(3r_1+r_2)C_T & 0 & 0 & (r_1+r_2)C_T & 0 & 0\\ 0 & (3r_1+r_2)C_T & 0 & 0 & (r_1+r_2)C_T & 0\\ 0 & 0 & (3r_1+r_2)C_N & 0 & 0 & (r_1+r_2)C_N\\ (r_1+r_2)C_T & 0 & 0 & (r_1+3r_2)C_T & 0 & 0\\ 0 & (r_1+r_2)C_T & 0 & 0 & (r_1+3r_2)C_T & 0\\ 0 & 0 & (r_1+r_2)C_N & 0 & 0 & (r_1+3r_2)C_N\end{bmatrix}\end{aligned} \tag{36}$$

in which L is the length of the element concerned, and $r(\eta)=(1-\eta)r_1/2+(1+\eta)r_2/2$, with r_i being the global r-coordinate of node i (i=1, 2) of the element concerned.

Similarly, the stiffness and damping matrices of the artificial boundary element on either of the two lateral boundaries shown in Fig. 5 can be derived:

$$\mathbf{K}^e_{\text{boundary}}=\frac{L}{6}\times\begin{bmatrix}2r_0k_N & 0 & 0 & r_0k_N & 0 & 0\\ 0 & 2r_0k_T & 0 & 0 & r_0k_T & 0\\ 0 & 0 & 2r_0k_T & 0 & 0 & r_0k_T\\ r_0k_N & 0 & 0 & 2r_0k_N & 0 & 0\\ 0 & r_0k_T & 0 & 0 & 2r_0k_T & 0\\ 0 & 0 & r_0k_T & 0 & 0 & 2r_0k_T\end{bmatrix} \tag{37}$$

$$\mathbf{C}^e_{\text{boundary}}=\frac{L}{6}\times\begin{bmatrix}2r_0C_N & 0 & 0 & r_0C_N & 0 & 0\\ 0 & 2r_0C_T & 0 & 0 & r_0C_T & 0\\ 0 & 0 & 2r_0C_T & 0 & 0 & r_0C_T\\ r_0C_N & 0 & 0 & 2r_0C_N & 0 & 0\\ 0 & r_0C_T & 0 & 0 & 2r_0C_T & 0\\ 0 & 0 & r_0C_T & 0 & 0 & 2r_0C_T\end{bmatrix} \tag{38}$$

where r_0 is the global r-coordinate of the lateral artificial boundary.

2.2.3 Assembly of tunnel-soil model

Through assembling the stiffness, mass and damping matrices of all the finite elements that represent the whole tunnel-soil system, the governing equation of the whole tunnel-soil system in the wavenumber-frequency domain can be obtained as

$$[\mathbf{K}^g(k)+\mathrm{i}\omega\mathbf{C}^g-\omega^2\mathbf{M}^g]\tilde{\hat{\mathbf{U}}}^g(k,\omega)=\tilde{\hat{\mathbf{F}}}^g(k,\omega) \tag{39}$$

where the superscript g denotes the global FE model; $\tilde{\hat{\mathbf{U}}}^g(k,\omega)$ and $\tilde{\hat{\mathbf{F}}}^g(k,\omega)$ are the displacement and external force vectors of the tunnel-soil FE model, respectively; $\mathbf{M}^g$, $\mathbf{C}^g$, $\mathbf{K}^g(k)$ are respectively the global mass, damping and stiffness matrices. Specially, the artificial boundary elements have no contribution to $\mathbf{M}^g$, while the tunnel and soil four-node 2.5D elements have no contribution to $\mathbf{C}^g$. In addition, $\mathbf{K}^g(k)$ can be further expressed as follows:

$$\mathbf{K}^g(k)=\mathbf{K}_{11}^g+\mathrm{i}k\mathbf{K}_{12}^g-\mathrm{i}k\mathbf{K}_{21}^g+k^2\mathbf{K}_{22}^g+\mathbf{K}_{\mathrm{boudary}}^g \tag{40}$$

in which $\mathbf{K}_{ij}^g$ is the assembled stiffness matrix from the corresponding element stiffness matrix $\mathbf{K}_{ij}^e$, and $\mathbf{K}_{\mathrm{boudary}}^g$ is the stiffness matrix of the whole artificial boundary, which is assembled from the stiffness matrices of all the 2.5D consistent viscoelastic artificial boundary elements.

2.3 Motion of curved track

In this subsection, the motion of the curved track is discussed. The curved rails are modelled as two curved Euler beams, and their vertical, transverse, longitudinal and rotational motions are all taken into consideration. The rail pads are modelled as continuously distributed spring-damper elements, neglecting the pinned-pinned motion of the track and the longitudinal inhomogeneity of the track dynamic stiffness. Specifically, a longitudinal distributed spring-damper element and a transverse (relative to the rail) one both located at the middle of the rail bottom, together with two vertical (relative to the rail) ones located at the two edges of the rail bottom are introduced to account for the motions of the rail, as shown in Fig. 6 (for the convenience of expression, the continuously distributed longitudinal and transverse spring-damper elements are denoted as an integrated sign in the figure). The superelevation of the curved track which is associated with the incline of the tunnel base is also considered in the present model, and the superelevation angle is assumed to be α. For the convenience of discussing the motion of the curved track, a local coordinate system is introduced to each rail, with θ , Y, Z and φ respectively representing the longitudinal, transverse, vertical and rotational directions of the rail.

Based on the governing equations of motion of the curved Euler beam [39–41], the governing equations of the curved track in the wavenumber-frequency domain can be given according to the corresponding force analyses shown in Fig. 7:

(1) Motions of the left rail:

$$[m\omega^2-\frac{k^2E^*A}{R_L^2}]\tilde{\hat{u}}_{L\theta}-[\frac{\mathrm{i}kE^*A}{R_L^2}+\frac{E^*I_Z}{R_L^4}(\mathrm{i}k^3-\mathrm{i}k)]\tilde{\hat{u}}_{LY}=\tilde{\hat{f}}_{L\theta} \tag{41}$$

$$[\frac{E^*A}{R_L^2}ik]\tilde{\hat{u}}_{L\theta}-[\frac{E^*I_Z}{R_L^4}k^4-\frac{E^*I_Z}{R_L^4}k^2+\frac{E^*A}{R_L^2}-m\omega^2]\tilde{\hat{u}}_{LY}=\tilde{\hat{f}}_{LY}-\tilde{\hat{F}}_{LY} \tag{42}$$

$$[-\frac{E^*I_Y}{R_L^4}k^4 - \frac{G^*I_d}{R_L^4}k^2 + m\omega^2]\tilde{\hat{u}}_{LZ} + [\frac{E^*I_Y}{R_L^3}k^2 + \frac{G^*I_d}{R_L^3}k^2]\tilde{\hat{\varphi}}_L = \tilde{\hat{f}}_{LZ1} + \tilde{\hat{f}}_{LZ2} + \frac{\mathrm{i}k\tilde{\hat{f}}_{L\theta}a}{R_L} - \tilde{\hat{F}}_{LZ} \tag{43}$$

$$[\frac{E^*I_Y}{R_L^3}(-\mathrm{i}k) - \frac{G^*I_d}{R_L^3}k^2]\tilde{\hat{u}}_{LZ} + [\frac{E^*I_Y}{R_L^2} + \frac{G^*I_d}{R_L^2}k^2 - \rho I_0\omega^2]\tilde{\hat{\varphi}}_L = b\tilde{\hat{f}}_{LZ1} - b\tilde{\hat{f}}_{LZ2} - a\tilde{\hat{f}}_{LY} + \tilde{\hat{M}}_{L\varphi} \tag{44}$$

(2) Motions of the right rail:

$$[m\omega^2 - \frac{k^2E^*A}{R_R^2}]\tilde{\hat{u}}_{R\theta} - [\frac{\mathrm{i}kE^*A}{R_R^2} + \frac{E^*I_Z}{R_R^4}(\mathrm{i}k^3 - \mathrm{i}k)]\tilde{\hat{u}}_{RY} = \tilde{\hat{f}}_{R\theta} \tag{45}$$

$$[\frac{E^*A}{R_R^2}\mathrm{i}k]\tilde{\hat{u}}_{R\theta} - [\frac{E^*I_Z}{R_R^4}k^4 - \frac{E^*I_Z}{R_R^4}k^2 + \frac{E^*A}{R_R^2} - m\omega^2]\tilde{\hat{u}}_{RY} = \tilde{\hat{f}}_{RY} - \tilde{\hat{F}}_{RY} \tag{46}$$

$$[-\frac{E^*I_Y}{R_R^4}k^4 - \frac{G^*I_d}{R_R^4}k^2 + m\omega^2]\tilde{\hat{u}}_{RZ} + [\frac{E^*I_Y}{R_R^3}k^2 + \frac{G^*I_d}{R_R^3}k^2]\tilde{\hat{\varphi}}_R = \tilde{\hat{f}}_{RZ1} + \tilde{\hat{f}}_{RZ2} + \frac{\mathrm{i}k\tilde{\hat{f}}_{R\theta}a}{R_R} - \tilde{\hat{F}}_{RZ} \tag{47}$$

$$[\frac{E^*I_Y}{R_R^3}(-\mathrm{i}k) - \frac{G^*I_d}{R_R^3}k^2]\tilde{\hat{u}}_{RZ} + [\frac{E^*I_Y}{R_R^2} + \frac{G^*I_d}{R_R^2}k^2 - \rho I_0\omega^2]\tilde{\hat{\varphi}}_R = b\tilde{\hat{f}}_{RZ1} - b\tilde{\hat{f}}_{RZ2} - a\tilde{\hat{f}}_{RY} + \tilde{\hat{M}}_{R\varphi} \tag{48}$$

where the shear centre of the cross section of the rail is assumed to coincide with its centroid, and the effect of cross-sectional warping is neglected due to the fact that the rail radius is much larger than the dimensions of the rail cross section. The meanings of symbols in Eqs. (41)–(48) are as follows: the first subscript *L* or *R* denotes the left rail or the right rail, while the second subscript denotes the direction in which the displacement occurs; $\tilde{\hat{u}}_{ij}$ (*i*=*L* or *R*; *j*=θ, *X*, or *Y*) is the displacement of left or right rail in the *j* direction, and $\tilde{\hat{\varphi}}_i$ (*i*=*L* or *R*) is the rotational displacement of left or right rail; R_i (*i*=*L* or *R*) is the radius of the left or right rail, which is equal to the radius *R* subtracting or adding the half of the track gauge; $E^* = E[1 + 2\mathrm{i}\xi\,\mathrm{sgn}(\omega)]$ and $G^* = G[1 + 2\mathrm{i}\xi\,\mathrm{sgn}(\omega)]$ are respectively the complex Young's modulus and shear modulus of the rail considering the material damping, with E, G and ξ being respectively the real Young's modulus, real shear modulus and damping ratio of the rail; ρ is the rail density, A is the cross-sectional area of the rail, and $m = \rho A$ is the mass per unit length of the rail; I_d is the torsional constant, I_0 is the rail's polar moment of area about the centroid of the cross-section, and I_Y and I_Z are respectively the rail's second moments of area with respect to *Y* axis and *Z* axis; $\tilde{\hat{f}}_{i\theta}$, $\tilde{\hat{f}}_{iY}$, $\tilde{\hat{f}}_{iZ1}$ and $\tilde{\hat{f}}_{iZ2}$ (*i*=*L* or *R*) are the reaction forces of the tunnel base to the left or right rail in the corresponding direction; $\tilde{\hat{F}}_{iY}$, $\tilde{\hat{F}}_{iZ}$ and $\tilde{\hat{M}}_{i\varphi}$ (*i*=*L* or *R*) are the external forces or moment applied to the left or right rail; *a* is the distance between the rail centroid and the rail bottom, and *b* is the half width of the rail bottom.

2.4 Coupling of track and tunnel-soil system

To simplify the coupling of the track and the tunnel-soil system, the longitudinal and transverse (relative to the rail) distributed spring-damper elements of each rail are both installed to connect a common node of two neighbouring four-node 2.5D finite elements accounting for a small part of the tunnel base. Due to the small width of the rail bottom, the two vertical (relative to the rail) distributed spring-damper elements located at the two edges of the left or right rail bottom are installed to connect two particular points on the two neighbouring edges of the corresponding two neighbouring elements which have been associated with the corresponding longitudinal and transverse spring-damper elements. In brief, the forces transmitted to the tunnel-soil system from the left or right rail are all made to act on the two neighbouring edges of two particular neighbouring four-node 2.5D finite elements accounting for a small part of the tunnel base. The detailed distribution of these forces acting on the tunnel-soil FE model which also corresponds to that of the continuously distributed spring-damper elements connecting the rails to the tunnel-soil FE model can be seen in Fig. 7.

With the node numbers of the three nodes of the two neighbouring edges in the tunnel-soil FE model corresponding to the left and right rails respectivley denoted as p_L, q_L and w_L, and p_R, q_R and w_R for the right rail (as shown in Fig. 7), the forces transmitted to the tunnel-soil system from the rails (or the reaction forces of the tunnel base to the rails) can be expressed as

$$\tilde{\hat{f}}_{L\theta} = (k_\theta + \mathrm{i}\omega c_\theta)(\tilde{\hat{u}}_{L\theta} - \tilde{\hat{U}}^g_{3q_L-1}), \tag{49a}$$

$$\tilde{\hat{f}}_{LY} = (k_Y + \mathrm{i}\omega c_Y)(\tilde{\hat{u}}_{LY} + a\tilde{\hat{\varphi}}_L - \tilde{\hat{U}}^g_{3q_L}\alpha - \tilde{\hat{U}}^g_{3q_L-2}), \tag{49b}$$

$$\begin{aligned}\tilde{\hat{f}}_{LZ1} &= (k_Z + \mathrm{i}\omega c_Z)(\tilde{\hat{u}}_{LZ} - b\tilde{\hat{\varphi}}_L - \tilde{\hat{u}}^b_{Lz1} + \tilde{\hat{u}}^b_{Lr1}\alpha) \\ &= (k_Z + \mathrm{i}\omega c_Z)\left\{\tilde{\hat{u}}_{LZ} - b\tilde{\hat{\varphi}}_L - [(1-\beta_{L1})\tilde{\hat{U}}^g_{3p_L} + \beta_{L1}\tilde{\hat{U}}^g_{3q_L}] + [(1-\beta_{L1})\tilde{\hat{U}}^g_{3p_L-2} + \beta_{L1}\tilde{\hat{U}}^g_{3q_L-2}]\alpha\right\},\end{aligned} \tag{49c}$$

$$\begin{aligned}\tilde{\hat{f}}_{LZ2} &= (k_Z + \mathrm{i}\omega c_Z)(\tilde{\hat{u}}_{LZ} + b\tilde{\hat{\varphi}}_L - \tilde{\hat{u}}^b_{Lz2} + \tilde{\hat{u}}^b_{Lr2}\alpha) \\ &= (k_Z + \mathrm{i}\omega c_Z)\left\{\tilde{\hat{u}}_{LZ} + b\tilde{\hat{\varphi}}_L - [(1-\beta_{L2})\tilde{\hat{U}}^g_{3q_L} + \beta_{L2}\tilde{\hat{U}}^g_{3w_L}] + [(1-\beta_{L2})\tilde{\hat{U}}^g_{3q_L-2} + \beta_{L2}\tilde{\hat{U}}^g_{3w_L-2}]\alpha\right\},\end{aligned} \tag{49d}$$

$$\tilde{\hat{f}}_{R\theta} = (k_\theta + \mathrm{i}\omega c_\theta)(\tilde{\hat{u}}_{R\theta} - \tilde{\hat{U}}^g_{3q_R-1}), \tag{49e}$$

$$\tilde{\hat{f}}_{RY} = (k_Y + \mathrm{i}\omega c_Y)(\tilde{\hat{u}}_{RY} + a\tilde{\hat{\varphi}}_R - \tilde{\hat{U}}^g_{3q_R}\alpha - \tilde{\hat{U}}^g_{3q_R-2}), \tag{49f}$$

$$\begin{aligned}\tilde{\hat{f}}_{RZ1} &= (k_Z + \mathrm{i}\omega c_Z)(\tilde{\hat{u}}_{RZ} - b\tilde{\hat{\varphi}}_R - \tilde{\hat{u}}^b_{Rz1} + \tilde{\hat{u}}^b_{Rr1}\alpha) \\ &= (k_Z + \mathrm{i}\omega c_Z)\left\{\tilde{\hat{u}}_{RZ} - b\tilde{\hat{\varphi}}_R - [(1-\beta_{R1})\tilde{\hat{U}}^g_{3p_R} + \beta_{R1}\tilde{\hat{U}}^g_{3q_R}] + [(1-\beta_{R1})\tilde{\hat{U}}^g_{3p_R-2} + \beta_{R1}\tilde{\hat{U}}^g_{3q_R-2}]\alpha\right\},\end{aligned} \tag{49g}$$

$$\begin{aligned}\tilde{\hat{f}}_{RZ2} &= (k_Z + \mathrm{i}\omega c_Z)(\tilde{\hat{u}}_{RZ} + b\tilde{\hat{\varphi}}_R - \tilde{\hat{u}}^b_{Rz2} + \tilde{\hat{u}}^b_{Rr2}\alpha) \\ &= (k_Z + \mathrm{i}\omega c_Z)\left\{\tilde{\hat{u}}_{RZ} + b\tilde{\hat{\varphi}}_R - [(1-\beta_{R2})\tilde{\hat{U}}^g_{3q_R} + \beta_{R2}\tilde{\hat{U}}^g_{3w_R}] + [(1-\beta_{R2})\tilde{\hat{U}}^g_{3q_R-2} + \beta_{R2}\tilde{\hat{U}}^g_{3w_R-2}]\alpha\right\}.\end{aligned} \tag{49h}$$

where k_j and c_j (j=θ, Y, Z, φ) are the stiffness and damping of the spring-damper element in the corresponding direction, respectively; $\tilde{\hat{u}}^b_{pji}$ is the j-direction (j=r, z) displacement of the tunnel base points connected by the i-th (i=1,2) vertical (relative to the rail) spring-damper element of the left (p=L) or right rail (p=R); $\beta_{L1} = 1 - b/L_{L1}$, $\beta_{L2} = b/L_{L2}$, $\beta_{R1} = 1 - b/L_{R1}$, and $\beta_{R2} = b/L_{R2}$; L_{L1}, L_{L2}, L_{R1} and L_{R2} are respectively the distances between nodes p_L and q_L, q_L and w_L, p_R and q_R, and q_R and w_R, as shown in Fig. 7; $\tilde{\hat{U}}^g_j$ is the j-th element of the displacement vector $\hat{\mathbf{U}}^g$ of the tunnel-soil FE model.

Substituting Eq. (49) into Eqs. (41)–(48), yields the following equation:

$$\begin{bmatrix}\mathbf{A}_{11} & \mathbf{A}_{12}\end{bmatrix}\begin{bmatrix}\tilde{\hat{\mathbf{U}}}^{t} \\ \tilde{\hat{\mathbf{U}}}^{g}\end{bmatrix}=\tilde{\hat{\mathbf{F}}} \tag{50}$$

where $\tilde{\hat{\mathbf{U}}}^{t}=[\tilde{\hat{u}}_{L\theta},\tilde{\hat{u}}_{LY},\tilde{\hat{u}}_{LZ},\tilde{\hat{\varphi}}_{L},\tilde{\hat{u}}_{R\theta},\tilde{\hat{u}}_{RY},\tilde{\hat{u}}_{RZ},\tilde{\hat{\varphi}}_{R}]^{T}$ and $\tilde{\hat{\mathbf{F}}}=[0,\tilde{\hat{F}}_{LY},\tilde{\hat{F}}_{LZ},\tilde{\hat{M}}_{L\varphi},0,\tilde{\hat{F}}_{RY},\tilde{\hat{F}}_{RZ},\tilde{\hat{M}}_{R\varphi}]^{T}$ are the track displacement vector and the external load vector acting on the track, respectively; $\mathbf{A}_{11}$ with the order 8×8 and $\mathbf{A}_{12}$ with the order $8\times N$ (in which N is the total number of DoFs of the 2.5D tunnel-soil FE model) are the known coefficient matrices.

On the other hand, according to the forces transmitted to the tunnel-soil system from the track, the equivalent nodal external forces at nodes p_L, q_L, w_L, p_R, q_R and w_R in the global coordinate system (r-θ-z coordinate system) of the 2.5D tunnel-soil FE model can be derived using Eq. (22) and corresponding coordinate transformation. Specifically, their expressions can be written as:

$$\tilde{\hat{F}}^{g}_{3p_L-2}=-(R_L-b)(1-\beta_{L1})\tilde{\hat{f}}_{LZ1}\alpha, \tag{51a}$$

$$\tilde{\hat{F}}^{g}_{3p_L-1}=0, \tag{51b}$$

$$\tilde{\hat{F}}^{g}_{3p_L}=(R_L-b)(1-\beta_{L1})\tilde{\hat{f}}_{LZ1}, \tag{51c}$$

$$\tilde{\hat{F}}^{g}_{3q_L-2}=R_L\tilde{\hat{f}}_{LY}-[(R_L-b)\beta_{L1}\tilde{\hat{f}}_{LZ1}+(R_L+b)(1-\beta_{L2})\tilde{\hat{f}}_{LZ2}]\alpha, \tag{51d}$$

$$\tilde{\hat{F}}^{g}_{3q_L-1}=R_L\tilde{\hat{f}}_{L\theta}, \tag{51e}$$

$$\tilde{\hat{F}}^{g}_{3q_L}=[(R_L-b)\beta_{L1}\tilde{\hat{f}}_{LZ1}+(R_L+b)(1-\beta_{L2})\tilde{\hat{f}}_{LZ2}]+R_L\tilde{\hat{f}}_{LY}\alpha, \tag{51f}$$

$$\tilde{\hat{F}}^{g}_{3w_L-2}=-(R_L+b)\beta_{L2}\tilde{\hat{f}}_{LZ2}\alpha, \tag{51g}$$

$$\tilde{\hat{F}}^{g}_{3w_L-1}=0, \tag{51h}$$

$$\tilde{\hat{F}}^{g}_{3w_L}=(R_L+b)\beta_{L2}\tilde{\hat{f}}_{LZ2}, \tag{51i}$$

$$\tilde{\hat{F}}^{g}_{3p_R-2}=-(R_R-b)(1-\beta_{R1})\tilde{\hat{f}}_{RZ1}\alpha, \tag{51j}$$

$$\tilde{\hat{F}}^{g}_{3p_R-1}=0, \tag{51k}$$

$$\tilde{\hat{F}}^{g}_{3p_R}=(R_R-b)(1-\beta_{R1})\tilde{\hat{f}}_{RZ1}, \tag{51l}$$

$$\tilde{\hat{F}}^{g}_{3q_R-2}=R_R\tilde{\hat{f}}_{RY}-[(R_R-b)\beta_{R1}\tilde{\hat{f}}_{RZ1}+(R_R+b)(1-\beta_{R2})\tilde{\hat{f}}_{RZ2}]\alpha, \tag{51m}$$

$$\tilde{\hat{F}}^{g}_{3q_R-1}=R_R\tilde{\hat{f}}_{R\theta}, \tag{51n}$$

$$\tilde{\hat{F}}^{g}_{3q_R}=[(R_R-b)\beta_{R1}\tilde{\hat{f}}_{RZ1}+(R_R+b)(1-\beta_{R2})\tilde{\hat{f}}_{RZ2}]+R_R\tilde{\hat{f}}_{RY}\alpha, \tag{51o}$$

$$\tilde{\hat{F}}^{g}_{3w_R-2}=-(R_R+b)\beta_{R2}\tilde{\hat{f}}_{RZ2}\alpha, \tag{51p}$$

$$\tilde{\hat{F}}^{g}_{3w_R-1}=0, \tag{51q}$$

$$\tilde{\hat{F}}^{g}_{3w_R}=(R_R+b)\beta_{R2}\tilde{\hat{f}}_{RZ2}. \tag{51r}$$

where $\tilde{\hat{F}}^{g}_{j}$ is the j-th element of the external force vector $\tilde{\hat{\mathbf{F}}}^{g}(k,\omega)$ of the tunnel-soil FE model.

Substituting Eq. (49) into Eq. (51), then substituting the resultant equations into Eq. (39), the following equation can be derived after some rearrangements:

$$\begin{bmatrix}\mathbf{A}_{21} & \mathbf{A}_{22}\end{bmatrix}\begin{bmatrix}\tilde{\hat{\mathbf{U}}}^t \\ \tilde{\hat{\mathbf{U}}}^g\end{bmatrix} = \mathbf{0} \tag{52}$$

where $\mathbf{0}$ is a zero vector with the order $N \times 1$, and $\mathbf{A}_{21}$ with the order $N \times 8$ and $\mathbf{A}_{22}$ with the order $N \times N$ are the known coefficient matrices.

When Eq. (50) and Eq. (52) are combined, the governing equation of the coupled track-tunnel-soil model can be obtained:

$$\begin{bmatrix}\mathbf{A}_{11} & \mathbf{A}_{12} \\ \mathbf{A}_{21} & \mathbf{A}_{22}\end{bmatrix}\begin{bmatrix}\tilde{\hat{\mathbf{U}}}^t \\ \tilde{\hat{\mathbf{U}}}^g\end{bmatrix} = \begin{bmatrix}\tilde{\hat{\mathbf{F}}} \\ \mathbf{0}\end{bmatrix} \tag{53}$$

2.5 Expressions of external loads and solution of coupled track-tunnel-soil system

The external moving loads acting on the left rail can be expressed in the space-time domain as

$$F_{LY} = \sum_{j=1}^{n} P_{LYj}(t)\delta(R_L\theta - R_L v_\theta t - R_L\theta_j) \tag{54a}$$

$$F_{LZ} = \sum_{j=1}^{n} P_{LZj}(t)\delta(R_L\theta - R_L v_\theta t - R_L\theta_j) \tag{54b}$$

$$M_{L\varphi} = \sum_{j=1}^{n} P_{L\varphi j}(t)\delta(R_L\theta - R_L v_\theta t - R_L\theta_j) \tag{54c}$$

where v_θ is the angular velocity of the moving loads; P_{Lij} (i=Y, Z and φ) is the time-domain magnitude of the j-th external load acting in the i direction; θ_j is the initial θ coordinate of the j-th external load with the time-domain magnitude P_{Lij} at the initial time t=0 s; n is the number of the external loads acting in the corresponding direction. Because all of the external loads acting on the rail in different directions correspond to the train axles in reality, the load series in different directions are assumed to have the same space distribution and speed in Eq. (54).

Based on Eq. (54), the expressions of the external loads acting on the left rail in the wavenumber-frequency domain can then be written as:

$$\tilde{\hat{F}}_{LY} = \frac{1}{R_L}\sum_{j=1}^{n}\hat{P}_{LYj}(\omega - kv_\theta)\mathrm{e}^{\mathrm{i}k\theta_j} \tag{55a}$$

$$\tilde{\hat{F}}_{LZ} = \frac{1}{R_L}\sum_{j=1}^{n}\hat{P}_{LZj}(\omega - kv_\theta)\mathrm{e}^{\mathrm{i}k\theta_j} \tag{55b}$$

$$\tilde{\hat{M}}_{L\varphi} = \frac{1}{R_L}\sum_{j=1}^{n}\hat{P}_{L\varphi j}(\omega - kv_\theta)\mathrm{e}^{\mathrm{i}k\theta_j} \tag{55c}$$

Since the expressions of the external loads acting on the right rail and the left rail are similar, those corresponding to the right rail are omitted here for brevity. Substituting Eq. (55) and the corresponding external loads acting on the right rail into Eq. (53), the displacement responses of the coupled track-tunnel-soil system can be solved:

$$\tilde{\hat{\mathbf{U}}}^t = (\mathbf{A}_{11} - \mathbf{A}_{12}\mathbf{A}_{22}^{-1}\mathbf{A}_{21})^{-1}\tilde{\hat{\mathbf{F}}} \tag{56}$$

$$\tilde{\hat{\mathbf{U}}}^{g} = -\mathbf{A}_{22}^{-1}\mathbf{A}_{21}(\mathbf{A}_{11} - \mathbf{A}_{12}\mathbf{A}_{22}^{-1}\mathbf{A}_{21})^{-1}\tilde{\hat{\mathbf{F}}} \tag{57}$$

Applying the inverse Fourier transform with respect to wavenumber *k* to the above two equations, the corresponding displacement responses in the space-frequency domain can then be obtained:

$$\hat{\mathbf{U}}^{t} = \frac{1}{2\pi}\int_{-\infty}^{+\infty}(\mathbf{A}_{11} - \mathbf{A}_{12}\mathbf{A}_{22}^{-1}\mathbf{A}_{21})^{-1}\tilde{\hat{\mathbf{F}}}\mathrm{e}^{-\mathrm{i}k\theta}\mathrm{d}k \tag{58}$$

$$\hat{\mathbf{U}}^{g} = \frac{-1}{2\pi}\int_{-\infty}^{+\infty}\mathbf{A}_{22}^{-1}\mathbf{A}_{21}(\mathbf{A}_{11} - \mathbf{A}_{12}\mathbf{A}_{22}^{-1}\mathbf{A}_{21})^{-1}\tilde{\hat{\mathbf{F}}}\mathrm{e}^{-\mathrm{i}k\theta}\mathrm{d}k \tag{59}$$

Similarly, the displacement responses of the curved track-tunnel-soil system in the space-time domain can be derived through the double inverse Fourier transform:

$$\mathbf{U}^{t} = \frac{1}{(2\pi)^{2}}\int_{-\infty}^{+\infty}\int_{-\infty}^{+\infty}(\mathbf{A}_{11} - \mathbf{A}_{12}\mathbf{A}_{22}^{-1}\mathbf{A}_{21})^{-1}\tilde{\hat{\mathbf{F}}}\mathrm{e}^{-\mathrm{i}k\theta}\mathrm{e}^{\mathrm{i}\omega t}\mathrm{d}k\mathrm{d}\omega \tag{60}$$

$$\mathbf{U}^{g} = \frac{-1}{(2\pi)^{2}}\int_{-\infty}^{+\infty}\int_{-\infty}^{+\infty}\mathbf{A}_{22}^{-1}\mathbf{A}_{21}(\mathbf{A}_{11} - \mathbf{A}_{12}\mathbf{A}_{22}^{-1}\mathbf{A}_{21})^{-1}\tilde{\hat{\mathbf{F}}}\mathrm{e}^{-\mathrm{i}k\theta}\mathrm{e}^{\mathrm{i}\omega t}\mathrm{d}k\mathrm{d}\omega \tag{61}$$

Further, the corresponding velocity and acceleration responses of the curved track-tunnel-soil system can also be easily obtained according to the derived displacement responses.

3. Model validations

A MATLAB program is created for the present model. Using this program, the validations of the present model are carried out in this section. A special case of a half-space subjected to a load moving along a straight line and a curved track-tunnel-soil system subjected to a dynamic load exhibiting a rotational symmetry are respectively considered, followed by comprehensive comparisons between the simulated results computed by the present model and the corresponding benchmark solutions.

3.1 A half-space subjected to a load moving along a straight line

In the first validation, a uniform viscoelastic half-space subjected to a vertical (in the *z* direction) unit harmonic point load $f(t) = -\mathrm{e}^{\mathrm{i}(2\pi f_0)t}$ moving along a straight line on the surface of the half-space is considered. The load is assumed to be at $\theta = 0\ \text{rad}$ at the initial time $t = 0\ \text{s}$, and it is assumed to move at $v = 60\ \text{km/h}$. The viscoelastic half-space considered has a modulus of elasticity $E_m = 175\ \text{MPa}$, mass density $\rho_m = 1940\ \text{kg/m}^3$, Poisson's ratio $\upsilon_m = 0.439$ and material damping ratio $\xi_m = 0.04$. The present method and the analytical approach presented by Hung and Yang [6] are respectively adopted to compute this dynamic problem.

In the simulation of this dynamic problem using the present method, the track model is excluded and the radius of the load's moving trajectory *R* is set to be large enough ($R = 10000\ \text{m}$ is used here) so that the problem described by the present model can be approximately regarded as a typical dynamic problem where the load moves along a straight line. Based on this consideration, a curved 2.5D model with a width of 80 m (the distances from the loading point to the left and right boundaries in the *r* direction are both 40 m) and a depth of 60 m is established to simulate this problem. The sizes of the considered domain mentioned above are made sufficiently large to ensure the computational accuracy of the core range in the middle of the considered domain, considering that the viscoelastic boundaries adopted in the present model cannot completely eliminate the wave reflections at the FE mesh borders. The element sizes of this FE model are also made to be small enough for accurate simulation results.

The vertical and longitudinal displacements of the point 2 m beneath the load trajectory and 160 m from the load's initial position in the longitudinal direction computed by both the present model and the reference solution are depicted in Fig. 8. Two excitation frequencies of the load which are 0 Hz and 10 Hz are considered herein. As can be seen, the results obtained by the present approach are in good agreement with those obtained by the analytical solution. Actually, it can be found that the responses of an arbitrary point at a distance no smaller than 20 m to any artificial boundary computed by the established 2.5D model have very good accuracy. Thus, in the following analyses using the present 2.5D model, only the responses of the points at a distance no smaller than 20 m to any artificial boundary are considered.

3.2 A curved track-tunnel-soil system subjected to a distributed dynamic load

For a further validation of the present model, a curved track-tunnel-soil system subjected to a vertical stationary load $F_{LZ}(\theta,t) = -\cos(n\theta)\mathrm{e}^{\mathrm{i}(2\pi f_0)t}$ acting on the left rail is also considered. In this validation, the considered tunnel with a buried depth of 17 m is assumed to be a circular one and embedded in a homogeneous viscoelastic half-space. Its external and internal radii are respectively assumed to be 3 m and 2.7 m. The parameters of the tunnel-soil system are listed in Table 1. The horizontal radii of the curved track and the curved tunnel are both 300 m. The superelevation of the outer rail relative to the inner rail is 12 cm. The track with DTVI$_2$ fasteners which is the most commonly used track in Chinese metro is considered herein, and its parameters for the present model are listed in Table 2 according to the corresponding values reported in Ref. [41]. The present method, and a reference solution based on a 3D FE model combined with an assessment of the motion of a curved rail are respectively used to simulate the dynamic responses of the considered problem. The comparisons of the simulated results computed by these two methods are made for four loading conditions: (a) n=0, f_0=10 Hz; (b) n=60, f_0=10 Hz; (c) n=0, f_0=25 Hz and (d) n=60, f_0=25 Hz.

Since only the vertical (relative to the rail) loading condition is considered and the dynamic characteristics of a curved rail with a large radius and a straight rail are similar [35], the motion of the left rail in the reference solution is assessed using the curved rail model presented in Ref. [42]. Considering the continuous support of the curved rail, the motion of the left rail can be written as follows:

$$E^{*}I_{Y}\frac{\partial^{4}u_{LZ}}{R_{L}^{4}\partial\theta^{4}}+m\frac{\partial^{2}u_{LZ}}{\partial t^{2}}=-\cos(n\theta)\mathrm{e}^{\mathrm{i}(2\pi f_0)t}-k_{Z}^{'}(u_{LZ}-u_{LZ}^{b})-c_{Z}^{'}(\dot{u}_{LZ}-\dot{u}_{LZ}^{b}) \tag{62}$$

where the rail pads are modelled as a continuously distributed spring-damper element with a stiffness $k_Z^{'}$ and a damping $c_Z^{'}$. Obviously, the values of $k_Z^{'}$ and $c_Z^{'}$ should be set to be two times those of k_Z and

c_Z adopted in the corresponding curved 2.5D model which will be established soon for a direct comparison. u_{LZ}^b is the displacement response in the vertical direction of the rail at the tunnel base points connected by the distributed spring-damper element. The meanings of the other symbols in Eq. (62) are same as those in the curved track model presented in section 2.3.

Because the load acting on the rail is harmonic with respect to the θ-coordinate, the resulting u_{LZ}, u_{LZ}^b and displacement response of an observation point of the tunnel-soil system u_O are also harmonic:

$$u_{LZ} = \bar{u}_{LZ} \cos(n\theta) \mathrm{e}^{\mathrm{i}(2\pi f_0)t} \tag{63}$$

$$u_{LZ}^b = \bar{u}_{LZ}^b \cos(n\theta) \mathrm{e}^{\mathrm{i}(2\pi f_0)t} \tag{64}$$

$$u_O = \bar{u}_O \cos(n\theta) \mathrm{e}^{\mathrm{i}(2\pi f_0)t} \tag{65}$$

where $\bar{u}_{LZ}$, $\bar{u}_{LZ}^b$ and $\bar{u}_O$ are the corresponding amplitudes.

Substituting Eqs. (63)–(65) into Eq. (62), yields:

$$[E^* I_Y \frac{n^4}{R_L^4} - m(2\pi f_0)^2 + k_Z^{'} + \mathrm{i}c_Z^{'}(2\pi f_0)]\bar{u}_{LZ} - [k_Z^{'} + \mathrm{i}c_Z^{'}(2\pi f_0)]\bar{u}_{LZ}^b = 1 \tag{66}$$

On the other hand, the amplitude of the load transmitted to the tunnel base from the curved rail can be expressed as:

$$\bar{f}_{LZ} = [k_Z^{'} + \mathrm{i}c_Z^{'}(2\pi f_0)](\bar{u}_{LZ} - \bar{u}_{LZ}^b) \tag{67}$$

Based on $\bar{f}_{LZ}$, $\bar{u}_{LZ}^b$ and $\bar{u}_O$ can be further expressed as:

$$\bar{u}_{LZ}^b = \bar{f}_{LZ} \bar{u}_{LZ0}^b \tag{68}$$

$$\bar{u}_O = \bar{f}_{LZ} \bar{u}_{O0} \tag{69}$$

where $\bar{u}_{LZ0}^b$ and $\bar{u}_{O0}$ are respectively the displacement response amplitude of the tunnel base points connected by the spring-damper element and that of the observation point due to the unit distributed load $f(\theta,t) = -\cos(n\theta)\mathrm{e}^{\mathrm{i}(2\pi f_0)t}$ in the vertical direction of the rail directly acting on these tunnel base points connected by the distributed spring-damper element.

A 3D FE model employing the rotational symmetry condition of the concerned problem shown in Fig. 9 is established to compute $\bar{u}_{LZ0}^b$ and $\bar{u}_{O0}$. The ranges of this 3D FE model in the r, z and θ directions are from 240 m to 360 m (the distances from the tunnel centre line to the left and right boundaries are both 60 m), from –60 m to 0 m, and from 0 rad to $\pi/15$ rad, respectively. It should be emphasized that the size of the 3D FE model in the θ direction is equal to two times the periodic length of the external load in the same (θ) direction when n is set to 60. The left, right and bottom boundaries are modelled as lumped viscoelastic boundaries, and the stiffness or damping of the spring-damper element in a particular direction at any boundary node is set to be the product of the corresponding parameter of the consistent viscoelastic boundary adopted in the proposed curved 2.5D model and the area of the boundary region corresponding to the node concerned. The front and back boundaries which are normal to the θ direction are modelled as rotational symmetry boundaries. After $\bar{u}_{LZ0}^b$ and $\bar{u}_{O0}$ are computed, through Eq. (65) to Eq. (69), the desired response u_O can be derived.

In the simulation of this dynamic problem using the proposed 2.5D method, a curved 2.5D model with the same cross section of the above 3D FE model is established. Similar to the solution of the curved track-tunnel-soil system under a moving load, the responses of the curved track-tunnel-soil system under the distributed stationary load can be directly solved after substitution of the expression of the external load in the wavenumber-frequency domain into Eqs. (56)–(61).

The dynamic responses of ground surface points V1 and V2 (shown in Fig. 9) that are on the cross section plane $\theta = \pi/30\ \mathrm{rad}$ and have a distance 40 m from the tunnel centre line on both the inner and outer sides of the curved tunnel are investigated. Fig. 10 depicts the real parts of the vertical displacements of these two observation points obtained by both the present model and the reference solution. It can be found that the results obtained by the present approach are in good agreement with those obtained by the reference solution for all the loading conditions. The slight differences between the corresponding results obtained by these two methods are mainly attributed to the different track models and boundary models adopted in them. Thus, the proposed curved 2.5D model is well verified.

4. Numerical examples

In this section, some numerical examples of the proposed model are given and the differences between the dynamic features of the straight and curved track-tunnel-soil systems are discussed. To investigate and clarify the effects of the curvature of the track-tunnel system and the track superelevation on the ground vibrations, three coupled track-tunnel-soil systems with different curvatures and superelevations are considered herein. They are a curved track-tunnel-soil system with a horizontal radius $R = 400\ \mathrm{m}$ and a superelevation angle $\alpha = 0.084\ \mathrm{rad}$ (the corresponding superelevation of the outer rail relative to the inner rail is 12 cm), a straight track-tunnel-soil system with no superelevation, and a straight track-tunnel-soil system but with a superelevation angle $\alpha = 0.084\ \mathrm{rad}$ (same as that in the curved case) which is taken as a transition case between the other two cases. The tunnels in the three cases are assumed to have the same circular cross-section with an internal radius of 2.7 m and a wall thickness of 0.3 m. Meanwhile, the tunnel base in the second case is assumed to have the same shape as those in the other two cases, and the only difference between them is a rotation angle around the circular tunnel centre. The other structural configurations in the three cases not mentioned above are also set to be the same in the present work. Specifically, in each case, the buried depth of the tunnel is assumed to be 15.6 m, and the ground is assumed to be comprised of three soil layers which are respectively the fill material, silty clay, and pebbles and gravels, as shown in Fig. 11. The parameters of each soil layer are listed in Table 3, while the parameters of the tunnel base, tunnel lining and track in the considered three structural configuration cases are the same as those listed in Table 1 and Table 2. The harmonic point loads $P_{Lj}(t) = -\cos(2\pi f_0 t)$ in *j* (*j*=*Y*, *Z* and φ) direction with a moving speed of 60 km/h ($v_\theta = 0.0417\ \mathrm{rad/s}$) equal to the normal operation speed of metro trains in China acting on the left rail are considered in each case, serving as the dynamic excitations in the following numerical examples.

All of the three structural configuration cases are simulated using the present model. In particular, the simulation of the two straight cases using the present model is achieved by setting the radius R to be 10000 m which is large enough for an appropriate approximation of the straight case. To ensure the accuracy of simulation results below 80 Hz, three curved 2.5D FE models are respectively established for these considered cases according to the rule of thumb that a minimum of six elements per wavelength is necessary for an accurate finite element solution. These FE models are all designed to have a width of 160 m (the distances from the tunnel centre line to the left and right boundaries in the r direction are both 80 m, i.e. the r coordinates of the left and right boundaries are respectively R−80 and R+80) and a depth of 70 m. This considered domain is selected based on the research presented in Section 3.1, and such a selection aims at ensuring the computational accuracy of the ground surface points in the range $r \in [R-60, R+60]$. Fig. 12 shows the mesh of the established 2.5D FE model accounting for the curved case and the straight case with a superelevation angle $\alpha = 0.084\ \text{rad}$ (the same FE mesh is used to analyse these two cases). The FE mesh for the straight case with no superelevation is similar to that shown in Fig. 12, thus its schematic diagram is omitted here. In the following simulations, the initial positions of the moving loads at $t = 0\ \text{s}$ are all assumed to be at $\theta = 0\ \text{rad}$, and the responses of the ground surface points on the cross section plane $\theta = 250/R$ are investigated. On the concerned cross section plane, the symbols "I-j" and "O-n" are respectively introduced to represent the points inside and outside radius R of the tunnel, as shown in Fig. 11. Numbers j and n denote the distances between the concerned points and the ground surface point I-0 (or O-0) just above the tunnel centre. For convenience, the points inside or outside radius R are called inner side points or outer side points in the present paper. In the following analyses, 4097 sampling frequency points uniformly distributed in the frequency range 0–80 Hz are calculated for each considered case (i.e. a particular structural configuration case subjected to a particular dynamic excitation). It is worth noting that the computation times of all the considered cases for each sampling frequency on average only need about 7 s using a PC with 16 GB RAM and four 3.50 GHz processors, even though large FE models (more than 110000 DoFs) are considered here. It is thus clear that the proposed model can efficiently simulate the dynamic track-tunnel-soil interaction in the curved section.

Figs. 13 and 14 depict the ground surface vertical acceleration spectrums of the considered three structural configuration cases due to the unit harmonic moving load $P_{LZ}(t) = -\cos(2\pi f_0 t)$ with excitation frequencies of $f_0 = 20\ \text{Hz}$ and $f_0 = 40\ \text{Hz}$, respectively. The responses of points I-10, I-60, O-10 and O-60 are shown in these figures. It can be clearly seen from Figs. 13 and 14 that the frequency-domain acceleration responses of the ground surface due to the harmonic moving load acting on the rail concentrate in a narrow frequency band around the excitation frequency f_0. Specifically, it is found that the frequency range of the ground vibration is mainly controlled by the S-wave speed of the second soil layer where the moving excitation source locates in the present case, given in the form $[f_0/(1+v/C_{S\_2}), f_0/(1-v/C_{S\_2})]$

(in which C_{S_2} is the S-wave speed of the second soil layer), i.e. [19.0 Hz, 21.1 Hz] for $f_0 = 20\ \text{Hz}$ and [38.0 Hz, 42.3 Hz] for $f_0 = 40\ \text{Hz}$, attributed to the Doppler effect present within the time duration when the load moves towards and recedes from the cross section containing the observation points [8]. Additionally, multiple peaks occur in the spectrums, and the peaks in different structural configuration cases under the same excitation load have favourable corresponding relationships. Based on the existing studies on the straight moving load problem [8], it can be easily deduced that these peaks occurring in the spectrums for all the curved and straight cases are attributed to the Doppler effects of different waves (P-waves, S-waves and R-waves) present in the multi-layer soils when the load moves towards and recedes from the cross section containing the observation points.

By comparing the responses of the two straight cases under the same excitation load in Figs. 13 and 14, it is found that the superelevation only influences the magnitude of the spectrum and its setting won't change the trend and the peak locations of the spectrum. However, the curvature of the track-tunnel system influences both the magnitude and the peak locations of the spectrum. In particular, an identifiable shift tendency of the peak location can be found in the spectrums of the curved case compared with the corresponding spectrums of the straight case with a superelevation angle $\alpha = 0.084$ rad which is the same as that in the curved case, especially in the spectrums of points I-60 and O-60 which are far away from the excitation source. Specifically, the shift directions of the spectrum peaks for an inner side point and an outer side point in the curved case are opposite: for the former one, the spectrum peaks will have a tendency to move towards the excitation frequency, whereas for the latter one, the spectrum peaks will have a tendency to move away from the excitation frequency. Obviously, this phenomenon can be attributed to the discrepancy between the trajectory of the moving load in the curved case and that in the straight case. Compared with the straight case, when the load moves towards or recedes from the concerned cross section, the instantaneous speed of the moving load relative to an inner side observation point at any time becomes smaller while that relative to an outer side observation point becomes greater. Hence, the spectrum peaks due to the Doppler effect in the curved case will have such tendencies relative to those in the corresponding straight case. It can be further noted that such tendencies of the curved case relative to the corresponding straight case are not obvious in the spectrums of points I-10 and O-10 which are near the tunnel.

This phenomenon can be explained as follows: for an observation point near the tunnel, only when the load moves into a small region in the longitudinal direction near the observation point can it have a decisive influence on the response of the observation point; however, the differences between the spatial positions of a straight track-tunnel system and a curved one in this small region are relatively small.

The influences of the curvature of the track-tunnel system on the ground-borne vibrations can also be found from Figs. 15 and 16, where the running root mean square values (RMS-values) of the vertical accelerations of the ground surface points I-60 and O-60 in the curved case and the straight case with the same superelevation due to $P_{LZ}(t) = -\cos(2\pi f_0 t)$ with $f_0 = 40\,\text{Hz}$ and $f_0 = 20\,\text{Hz}$ are respectively depicted. The running RMS-values shown in these two figures are calculated through the following equation:

$$a_{\text{RMS}}(t) = \sqrt{\frac{1}{T}\int_{t-T/2}^{t+T/2} [a(t)]^2 \,\mathrm{d}t} \tag{70}$$

where $a_{\text{RMS}}(t)$ is the running RMS-value, $a(t)$ is the acceleration time history, and T is the length of the running average window. Here $T = 0.5\,\text{s}$ is used in order to ensure the readability of the related figures.

The dynamic behaviour caused by the load that moves towards and recedes from the cross section containing the observation points is clearly exhibited in Figs. 15 and 16. The time-domain responses of a ground point far away from the tunnel centre line in the curved case and the same ground point in the corresponding straight case have similar trends. The major differences between them occur in the periods of time before and after the load reaches the concerned cross section containing the observation points ($t = 15\,\text{s}$), which directly reflects the differences between the spatial locations of the load's moving trajectories in the curved and straight cases. Generally speaking, compared with the corresponding straight case, the time-domain response waveform of an inner side point in the curved case is just like to be stretched, while that of an outer side point is just like to be compressed.

Figs. 17–19 show the RMS-values of the ground surface time-domain accelerations in the considered three structural configuration cases due to the unit harmonic moving loads $P_{Lj}(t) = -\cos(2\pi f_0 t)$ with $f_0 = 20\,\text{Hz}$ versus the distance from the tunnel centre line. It should be noted that the RMS-values depicted in these figures are computed according to the time-domain accelerations in the time range 0–32 s where the significant responses concentrate, thus they are presented just as a measure of the total signal energy. The loads acting in the vertical, transverse and rotational directions of the rail are all considered herein, and those values at points I-60, I-55, …, I-5, I-0 (or O-0), O-5, …, O-55 and O-60 are depicted in each figure.

The effects of the curvature of the track-tunnel system and the track superelevation on the ground vibrations are clearly visible in Figs. 17–19. The track superelevation has a certain degree of influence on the ground responses in the near filed of the excitation source, but such an influence decreases with the increase of the distance from the tunnel centre line in general. Conversely, the curvature of the track-tunnel system has a certain degree of influence on the far-field ground responses, whereas its influence on the near-field ground responses is usually small and sometimes can even be neglected, just as discussed above. As expected, the curvature of the track-tunnel system will generally increase the RMS magnitudes of accelerations at ground surface points on the inner side of the tunnel horizontal radius, but decrease those on the outer side of the tunnel horizontal radius. For instance, under the transverse load $P_{LY}(t) = -\cos(2\pi f_0 t)$ with $f_0 = 20\,\text{Hz}$ acting on the rail, the radial, longitudinal and vertical acceleration RMS-values of the point I-55 in the curved case respectively increase by 6.0%, 14.6% and 9.1% compared with the straight case with the same superelevation angle $\alpha = 0.084\ \mathrm{rad}$, while those of the point O-55 respectively decrease by 5.7%, 9.1% and 7.6%. Compared with the radial and vertical responses, the influences of the curvature of the track-tunnel system on the longitudinal response are relatively more significant from an overall perspective.

Due to the much more complex loading condition on the curved track in reality, the ground vibration characteristics under dynamic loads acting on the rail in its vertical and transverse directions, and even its rotational direction are all significant for the propagation of the train-induced ground vibration from a curved railway tunnel. Thus, the vibration characteristics of the considered coupled curved track-tunnel-soil system (the curved case) due to the unit point moving loads acting on the rail in its different directions are further studied.

Fig. 20 gives the attenuation curves of the acceleration RMS-values in the curved case along the ground surface under the harmonic moving loads $P_{Lj}(t) = -\cos(2\pi f_0 t)$ with excitation frequencies $f_0 = 20\ \mathrm{Hz}$ and $f_0 = 40\ \mathrm{Hz}$. The acceleration responses in the three normal directions of the cylindrical coordinates at the same ground surface points as considered in Figs. 17–19 are all depicted herein. It should be noted again that the corresponding RMS-values depicted in this figure are also computed according to the time-domain accelerations in the time range 0–32 s and presented just as a measure of the total signal energy. The attenuation mechanisms of vibrations in different directions can be easily found from Fig. 20. Under the harmonic moving load acting in the transverse (Y) or rotational (φ) direction of the rail, the ground surface vertical and longitudinal vibrations show a general trend of first increase and then decrease with the increase of the distance from the tunnel centre line, while the ground surface radial vibration shows a general trend of decrease with the increase of the distance from the tunnel centre line. However, under the harmonic moving load acting in the vertical (Z) direction of the rail, the opposite phenomena can be observed. It should be emphasized that there still exist some fluctuations in these overall trends stated above due to the natures of wave propagation.

By carefully observing Fig. 20, the following interesting vibration characteristics can also be seen: the magnitudes of the ground vibration responses induced by the unit harmonic moving moment acting on the rail in its rotational (φ) direction are comparable with those induced by the unit harmonic moving loads acting on the rail in its vertical (Z) and transverse (Y) directions; under the harmonic moving load with some specific excitation frequencies acting on the rail in its transverse (Y) or rotational (φ) direction, the radial acceleration responses can be significantly greater than the longitudinal and vertical ones at most points in a wide region of the ground surface. Actually, the second vibration characteristic is related to the excitation frequency of the load. Through further analyses, it is found that as long as the excitation frequency of the load is high enough (e.g. 20 Hz and 40 Hz are already high enough for the vertical load and rotational moment acting on the rail, respectively), this vibration phenomenon will occur. It should be noted that this vibration characteristic is also suspected to be related to the phenomenon that the train-induced radial ground-borne vibrations from a curved underground metro are far larger than those in the vertical direction in a wide region of the ground surface reported in Ref. [29]. Of course, this speculation still needs further verifications.

5. Conclusions

A curved 2.5D model for simulating the dynamic responses of a coupled track-tunnel-soil system in a curved section due to moving loads is presented. By assuming the curved track-tunnel-soil system to be invariant in the longitudinal direction, the curved 2.5D finite element method and the curved 2.5D analytical method are respectively proposed to model the motions of the tunnel-soil system and the track. The formulations of the four-node curved 2.5D finite elements and the curved 2.5D consistent viscoelastic boundary elements which are respectively used to model the tunnel and soil mediums and the computation boundaries are derived in detail. By accounting for the force balance and displacement compatibility conditions, the curved track with an analytical solution is coupled to the curved tunnel-soil system with a finite element solution, leading to the governing equation of motion of the whole curved track-tunnel-soil system. This proposed model is well validated through the comparisons of its simulation results with the corresponding reference results computed by other theoretical models. Numerical examples show that the proposed model can efficiently simulate the dynamic responses of the coupled track-tunnel-soil system in the curved section, which can be attributed to its significant reduction of the number of degrees-of-freedom for the concerned dynamic problem relative to a conventional 3D FE model. Through the analyses, the following conclusions are obtained:

1) The track superelevation has a certain degree of influence on the ground responses in the near field of the excitation source, but such an influence decreases with the increase of the distance from the tunnel centre line in general.

2) Under the same harmonic moving load acting on the rail, the locations of the peaks in the acceleration spectrums of an inner side ground point and an outer side ground point in a curved track-tunnel-soil system will respectively have tendencies to move towards and move away from the excitation frequency of the load, compared with those of the same points in the corresponding straight track-tunnel-soil system. This phenomenon is particularly prominent for the far-field ground points.

3) The curvature of the track-tunnel system generally increases the RMS magnitudes of accelerations at the inner side ground points but decreases those at the outer side ground points.

4) Under the harmonic moving load with a high enough excitation frequency acting on the rail in its transverse or rotational direction, the radial ground vibrations from a curved railway tunnel can be significantly greater than the longitudinal and vertical ones at most points in a wide region of the ground

surface.

The proposed curved 2.5D model is now only applicable to the deterministic external loads, but it can be extended to simulate the train-induced ground-borne vibrations from the curved underground metros by considering the dynamic train-track interaction. This effort is of great significance for the further understandings of the vibration characteristics of the curved underground metro section, and the corresponding studies are our next works.

Acknowledgments

The authors would like to acknowledge the financial supports for this work provided by the National Natural Science Foundation of China (N0. 51608456), the Fundamental Research Funds for the Central Universities (N0. 2682017CX003) and the China Scholarship Council.

References:

[1] M. Ma, W.N. Liu, C.Y. Qian, G.H. Deng, Y.D. Li, Study of the train-induced vibration impact on a historic Bell Tower above two spatially overlapping metro lines, Soil Dynamics and Earthquake Engineering 81 (1) (2016) 58–74. http://dx.doi.org/10.1016/j.soildyn.2015.11.007.

[2] S. Gupta, W.F. Liu, G. Degrande, G. Lombaert, W.N. Liu, Prediction of vibrations induced by underground railway traffic in Beijing, Journal of Sound and Vibration 310 (3) (2008) 608–630. http://dx.doi.org/10.1016/j.jsv.2007.07.016.

[3] P. Alves Costa, R. Calçada, A. Silva Cardoso, Influence of train dynamic modelling strategy on the prediction of track-ground vibrations induced by railway traffic, Proceedings of the Institution of Mechanical Engineers, Part F: Journal of Rail and Rapid Transit 226 (4) (2012) 434–450. http://dx.doi.org/10.1177/0954409711433686.

[4] G. Eason, The stresses produced in a semi-infinite solid by a moving surface force, International Journal of Engineering Sciences 2 (6) (1965) 581–609. http://dx.doi.org/10.1016/0020-7225(65)90038-8.

[5] F.C.P. de Barros, J.E. Luco, Response of a layered viscoelastic half-space to a moving point load, Wave Motion 19 (2) (1994) 189–210. http://dx.doi.org/10.1016/0165-2125(94)90066-3.

[6] H.H. Hung, Y.B. Yang, Elastic waves in visco-elastic half-space generated by various vehicle loads, Soil Dynamics and Earthquake Engineering 21 (1) (2001) 1–17. http://dx.doi.org/10.1016/S0267-7261(00)00078-6.

[7] E. Kausel, Fundamental solutions in elastodynamics: a compendium, Cambridge University Press, 2006.

[8] Y.M. Cao, H. Xia, G. Lombaert, Solution of moving-load-induced soil vibrations based on the Betti–Rayleigh Dynamic Reciprocal Theorem, Soil Dynamics and Earthquake Engineering 30 (6) (2010) 470–480. http://dx.doi.org/10.1016/j.soildyn.2010.01.003.

[9] L. Andersen, S.R.K. Nielsen, Reduction of ground vibration by means of barriers or soil improvement along a railway track, Soil Dynamics and Earthquake Engineering 25 (7–10) (2005) 701–716.

http://dx.doi.org/10.1016/j.soildyn.2005.04.007.

[10] C.J.C. Jones, D.J. Thompson, M. Petyt, Studies using a combined finite element and boundary element model for vibration propagation from railway tunnels, in: G. Guidati, H. Hunt, H. Heller, A. Heiss (Eds.), 7th International Congress on Sound and Vibration, Garmisch-Partenkirchen, Germany, July 2000, pp. 2703–2710.

[11] L. Andersen, C.J.C. Jones, Coupled boundary and finite element analysis of vibration from railway tunnels-a comparison of two and three-dimensional models, Journal of Sound and Vibration 293 (3) (2006) 611–625. http://dx.doi.org/10.1016/j.jsv.2005.08.044.

[12] Y.B. Yang, H.H. Hung, A parametric study of wave barriers for reduction of train-induced vibrations, International Journal for Numerical Methods in Engineering 40 (20) (1997) 3729–3747. http://dx.doi.org/10.1002/(SICI)1097-0207(19971030)40:20%3C3729::AID-NME236%3E3.0.CO;2-8.

[13] S. Gupta, G. Degrande, Modelling of continuous and discontinuous floating slab tracks in a tunnel using a periodic approach, Journal of Sound and Vibration 329 (8) (2010) 1101–1125. http://dx.doi.org/10.1016/j.jsv.2009.10.037.

[14] Y.B. Yang, H.H. Hung, A 2.5D finite/infinite element approach for modelling visco-elastic bodies subjected to moving loads, International Journal for Numerical Methods in Engineering 51 (11) (2001) 1317–1336. http://dx.doi.org/10.1002/nme.208.

[15] H.H. Hung, G.H. Chen, Y.B. Yang, Effect of railway roughness on soil vibrations due to moving trains by 2.5D finite/infinite element approach, Engineering Structures 57 (2013) 254–266. http://dx.doi.org/10.1016/j.engstruct.2013.09.031.

[16] X. Sheng, C.J.C. Jones, D.J. Thompson, Prediction of ground vibration from trains using the wavenumber finite and boundary element methods, Journal of Sound and Vibration 293 (3) (2006) 575–586. http://dx.doi.org/10.1016/j.jsv.2005.08.040.

[17] S. François, M. Schevenels, P. Galvin, G. Lombaert, G. Degrande, A 2.5D coupled FE-BE methodology for the dynamic interaction between longitudinally invariant structures and a layered halfspace, Computer Methods in Applied Mechanics and Engineering, 199 (23–24) (2010) 1536–1548. http://dx.doi.org/10.1016/j.cma.2010.01.001.

[18] H. Grundmann, K. Muller, Dynamic interaction of a plane elastically mounted on a tunnel, in: C. Soize, G.I. Schueller (Eds.), Proceedings of the 6th European Conference on Structural Dynamics: Eurodyn 2005, vol.3, Paris, France, September 2005, pp. 1273–1278.

[19] K. Muller, H. Grundmann, S. Lenz, Nonlinear interaction between a moving vehicle and a plate elastically mounted on a tunnel, Journal of Sound and Vibration 310 (3) (2008) 558–586. http://dx.doi.org/10.1016/j.jsv.2007.10.042.

[20] J.A. Forrest, H.E.M. Hunt, A three-dimensional tunnel model for calculation of train-induced ground vibration, Journal of Sound and Vibration 294 (4) (2006) 678–705. http://dx.doi.org/10.1016/j.jsv.2005.12.032.

[21] J.A. Forrest, H.E.M. Hunt, Ground vibration generated by trains in underground tunnels, Journal of Sound and Vibration 294 (4) (2006) 706–736. http://dx.doi.org/10.1016/j.jsv.2005.12.031.

[22] M.F.M. Hussein, H. Hunt, A numerical model for calculating vibration from a railway tunnel

embedded in a full-space, Journal of Sound and Vibration 305 (3) (2007) 401–431. http://dx.doi.org/10.1016/j.jsv.2007.03.068.

[23] G.Y. Gao, Q.S. Chen, J.F. He, F. Liu, Investigation of ground vibration due to trains moving on saturated multi-layered ground by 2.5D finite element method, Soil Dynamics and Earthquake Engineering 40 (11) (2012) 87–98. http://dx.doi.org/10.1016/j.soildyn.2011.12.003.

[24] S. François, M. Schevenels, G. Lombaert, G. Degrande, A two-and-a-half-dimensional displacement-based PML for elastodynamic wave propagation, International Journal for Numerical Methods in Engineering 90 (7) (2012) 819–837. http://dx.doi.org/10.1002/nme.3344.

[25] P. Lopes, P. Alves Costa, M. Ferraz, R. Calçada, A. Silva Cardoso, A numerical modeling of vibrations induced by railway traffic in tunnels: From the source to the nearby buildings, Soil Dynamics and Earthquake Engineering 61–62 (3) (2014) 269–285. http://dx.doi.org/10.1016/j.soildyn.2014.02.013.

[26] P. Lopes, P. Alves Costa, R. Calçada, A. Silva Cardoso, Influence of soil stiffness on building vibrations due to railway traffic in tunnels: Numerical study, Computers and Geotechnics 61 (1) (2014) 277–291. http://dx.doi.org/10.1016/j.compgeo.2014.06.005.

[27] D. Clouteau, M. Arnst, T.M. Al-Hussaini, G. Degrande, Freefield vibrations due to dynamic loading on a tunnel embedded in a stratified medium, Journal of Sound and Vibration 283 (1–2) (2005) 173–199. http://dx.doi.org/10.1016/j.jsv.2004.04.010.

[28] G. Degrande, D. Clouteau, R. Othman, M. Arnst, H. Chebli, R. Klein, P. Chatterjee, B. Janssens, A numerical model for ground-borne vibrations from underground railway traffic based on a periodic finite element-boundary element formulation, Journal of Sound and Vibration 293 (3) (2006) 645–666. http://dx.doi.org/10.1016/j.jsv.2005.12.023.

[29] Y. Yuan, W.N. Liu, W.F. Liu, Propagation law of ground vibration in the curve section of metro based on in-situ measurement, China Railway Science 33 (4) (2012)133–138. (in Chinese)

[30] X.J. Sun, Y. Yuan, M. Ma, W.N. Liu, Prediction of metro train-induced low frequency vibration responses in far field, Journal of vibration and shock 36 (4) (2017) 198–202. (in Chinese)

[31] J. Martínez-Casas, E. Di Gialleonardo, S. Bruni, L. Baeza, A comprehensive model of the railway wheelset-track interaction in curves, Journal of Sound and Vibration 333 (18) (2014) 4152–4169. http://dx.doi.org/10.1016/j.jsv.2014.03.032.

[32] E. Di Gialleonardo, F. Braghin, S. Bruni, The influence of track modelling options on the simulation of rail vehicle dynamics, Journal of Sound and Vibration 331 (19) (2012) 4246–4258. http://dx.doi.org/10.1016/j.jsv.2012.04.024.

[33] A. Matsumoto, Y. Sato, H. Ono, M. Tanimoto, Y. Oka, E. Miyauchi, Formation mechanism and countermeasures of rail corrugation on curved track, Wear 253 (1-2) (2002) 178–184. http://dx.doi.org/10.1016/S0043-1648(02)00097-2.

[34] W.F. Liu, L.L. Du, L.X. Ma, W.N. Liu, Study on dynamic response of curved track subjected to harmonic loads based on periodic structure theory, in: W.M. Zhai, K.C.P. Wang (Eds.), ICRT 2017: Railway Development, Operations, and Maintenance, Chengdu, China, July 2017, pp. 118–129.

[35] W.F. Liu, L.L. Du, W.N. Liu, D.J. Thompson, Dynamic response of a curved railway track subjected to harmonic loads based on periodic structure theory, Proceedings of the Institution of Mechanical

Engineers, Part F: Journal of Rail and Rapid Transit 232 (7) (2018) 1932–1950. http://dx.doi.org/10.1177/0954409718754470.

[36] X.C. Wang, M. Shao, Fundamental and numerical methods of finite element method, Tsinghua University Press, Beijing, 1997. (in Chinese)

[37] M. Priestley, Spectral Analysis and Time Series, Vol. 1, Academic Press, London, 1981.

[38] J.B. Liu, Y.X. Du, X.L. Du, Z.Y. Wang, J. Wu, 3D viscous-spring artificial boundary in time domain, Earthquake Engineering and Engineering Vibration 5 (1) (2006) 93–102. http://dx.doi.org/10.1007/s11803-006-0585-2.

[39] V.Z. Vlasov, Thin-wall elastic beams, National Science Foundation, Washington D.C., 1961.

[40] C.P. Heins, Bending and torsion of structural members, China Communications Press, Beijing, 1981. (in Chinese)

[41] L.L. Du, W.N. Liu, W.F. Liu, L.X. Ma, A study on curved track dynamic response under a fixed harmonic load, Journal of vibration and shock 36 (20) (2017) 233–239, 247. (in Chinese)

[42] L.L. Du, W.N. Liu, W.F. Liu, L.X. Ma, Study on dynamic characteristics of a curved track subjected to harmonic moving loads, Procedia Engineering, 199 (1) (2017) 2639–2644. http://dx.doi.org/10.1016/j.proeng.2017.09.511.

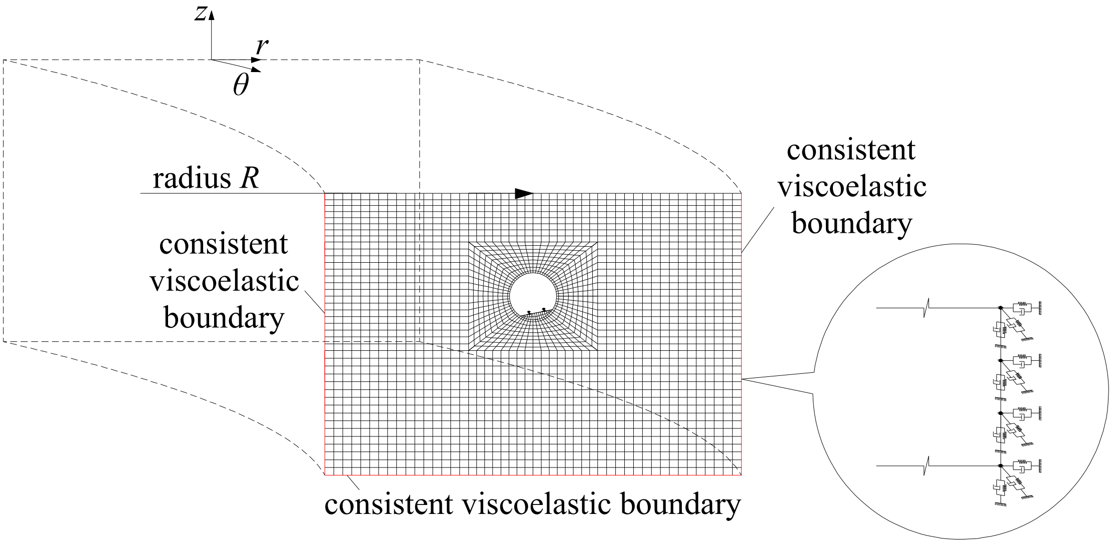

Fig. 1. 2.5D model representing the coupled curved track-tunnel-soil system.

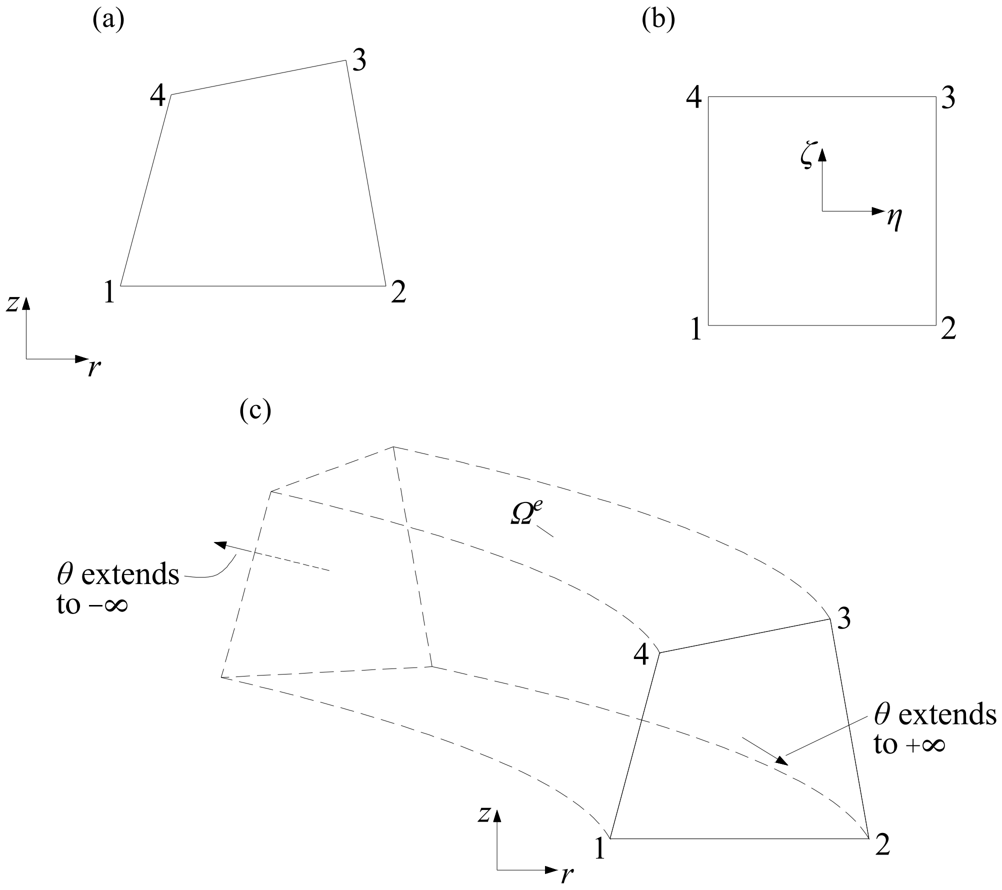

Fig. 2. Four-node curved 2.5D finite element and actual three-dimensional space represented by it: (a) the element in the global coordinate system; (b) the element in the local coordinate system; (c) the actual three-dimensional space represented by this element.

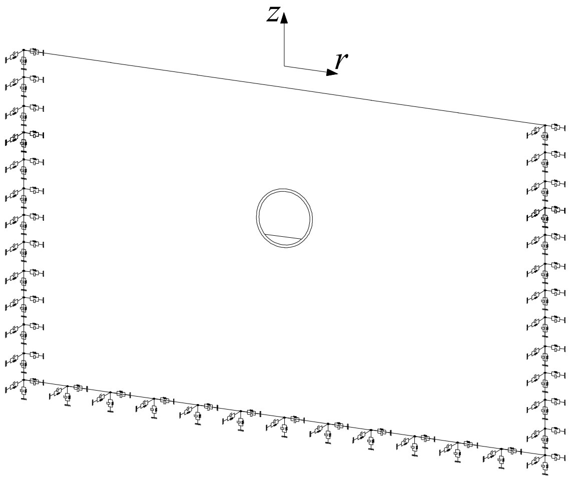

Fig. 3. 2.5D consistent viscoelastic artificial boundaries.

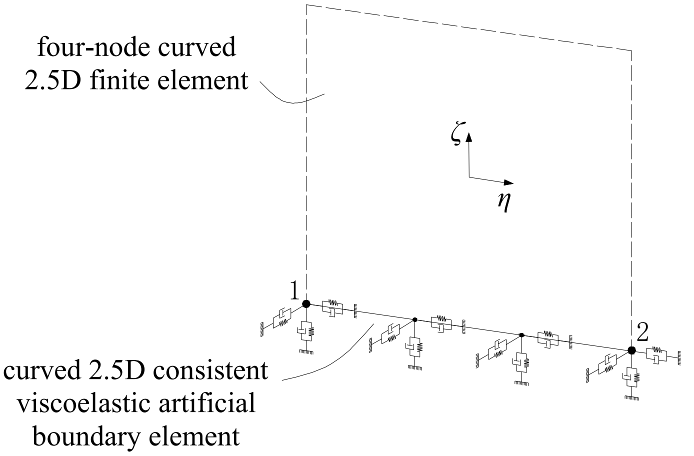

Fig. 4. Curved 2.5D consistent viscoelastic artificial boundary element at the bottom of the computation domain.

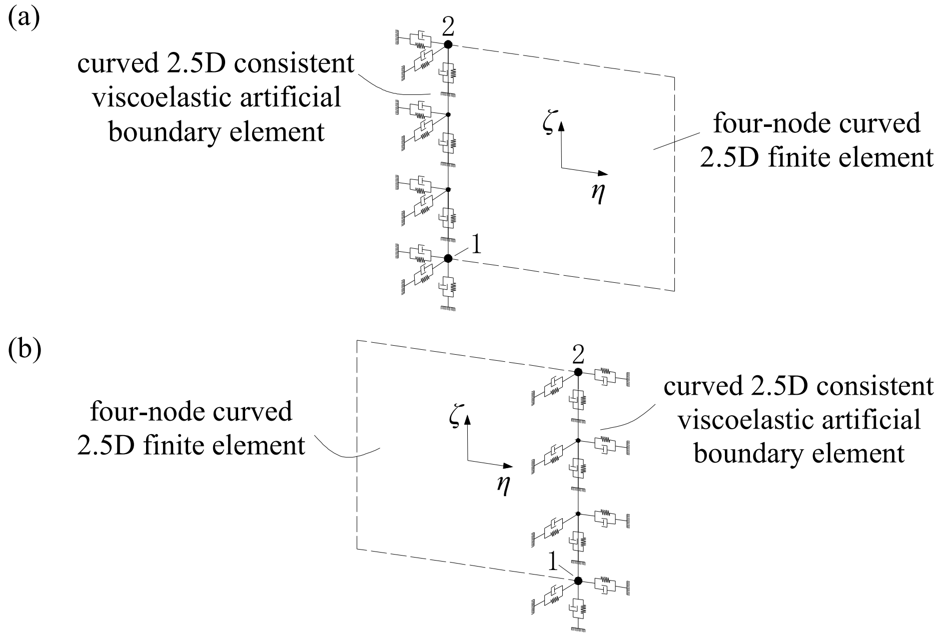

Fig. 5. Curved 2.5D consistent viscoelastic artificial boundary elements on the (a) left and (b) right lateral boundaries of the computation domain.

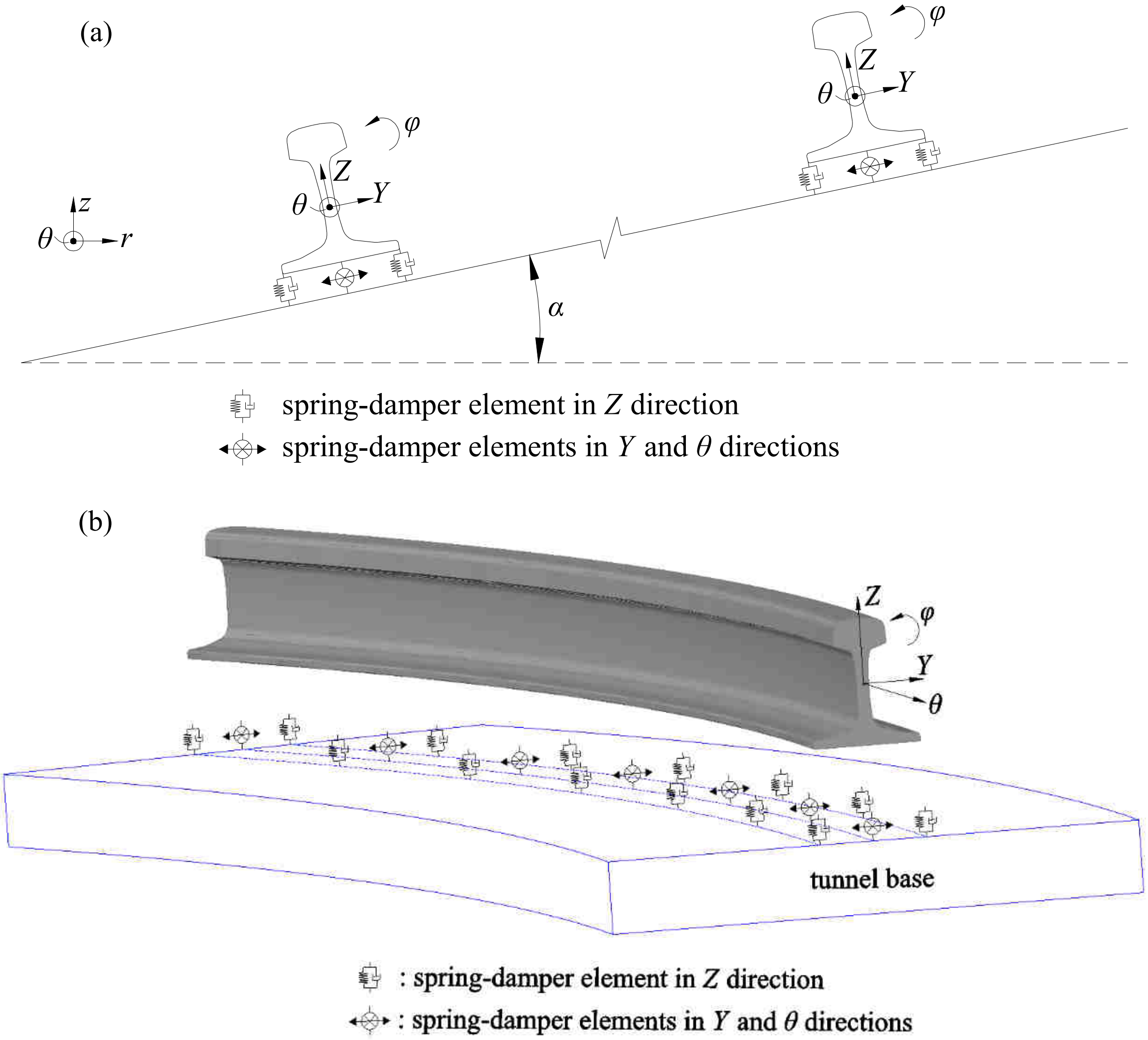

Fig. 6. Curved track model: (a) plane schematic diagram; (b) three dimensional schematic diagram.

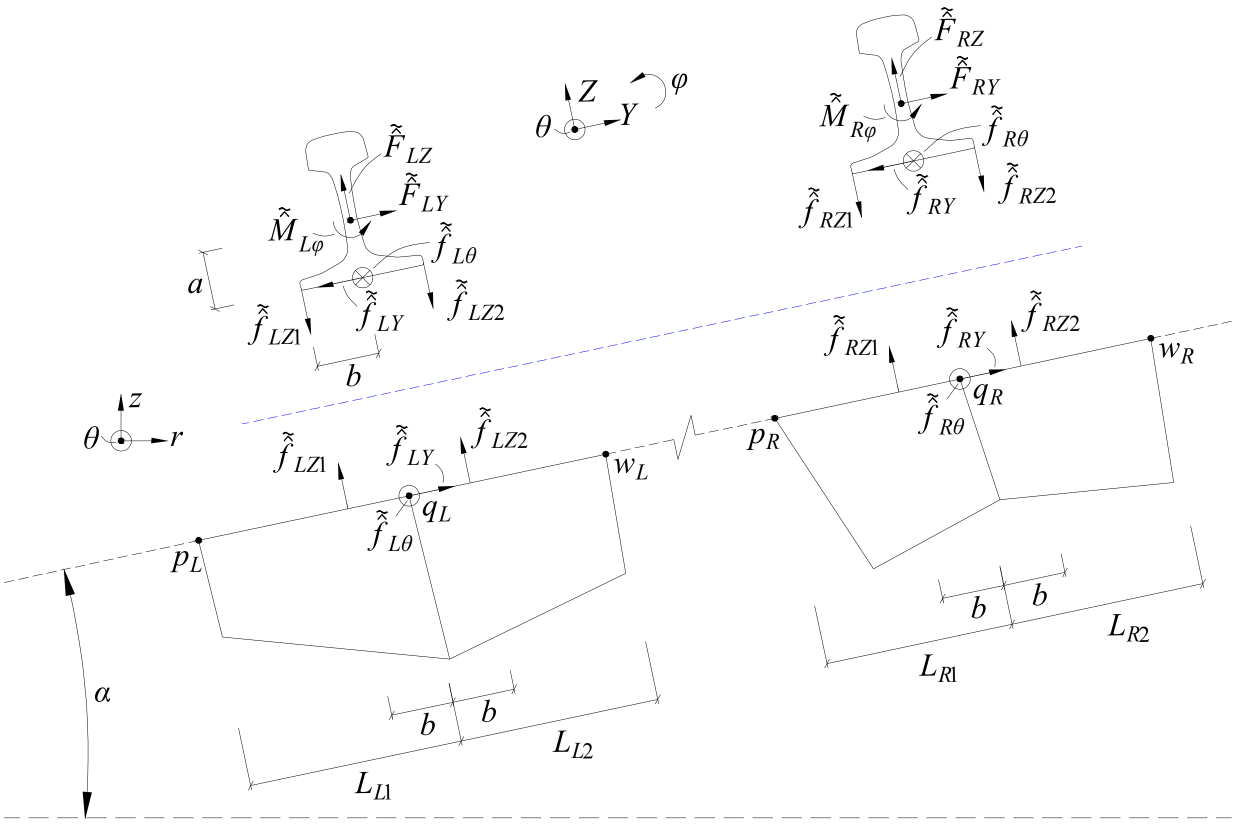

Fig. 7. Forces acting on the rails and the tunnel base.

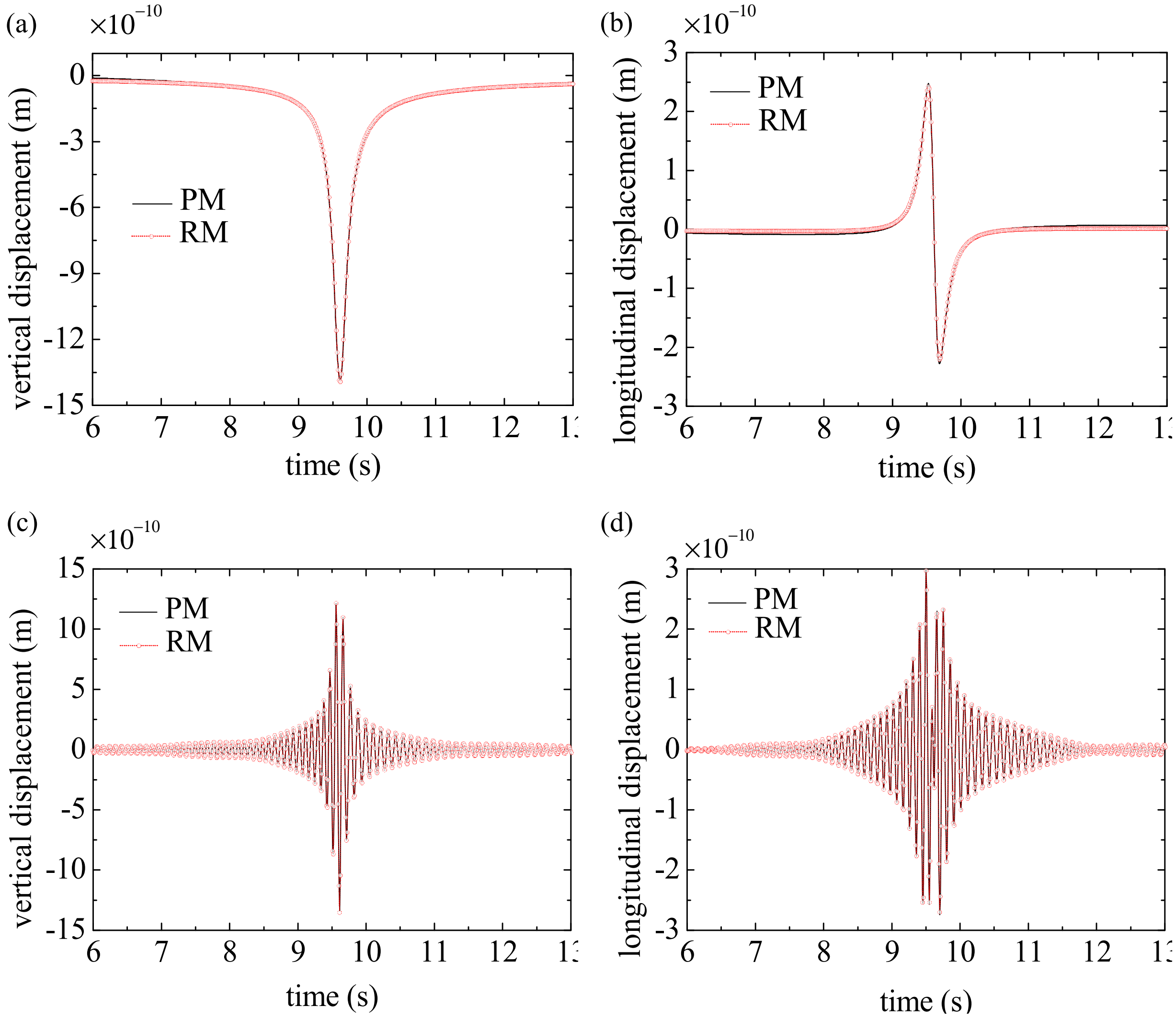

Fig. 8. Comparisons of the time-domain displacement responses of the uniform viscoelastic half-space induced by the moving point load $f(t)=-\mathrm{e}^{\mathrm{i}(2\pi f_0)t}$ computed by the present method (PM) and the reference method (RM): (a) vertical displacements under the excitation frequency f_0=0 Hz; (b) longitudinal displacements under the excitation frequency f_0=0 Hz; (c) vertical displacements under the excitation frequency f_0=10 Hz; (d) longitudinal displacements under the excitation frequency f_0=10 Hz.

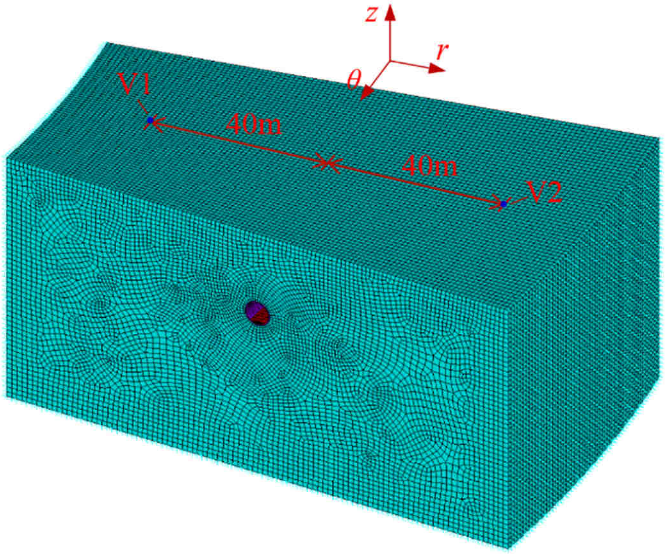

Fig. 9. 3D FE model established for the model validation.

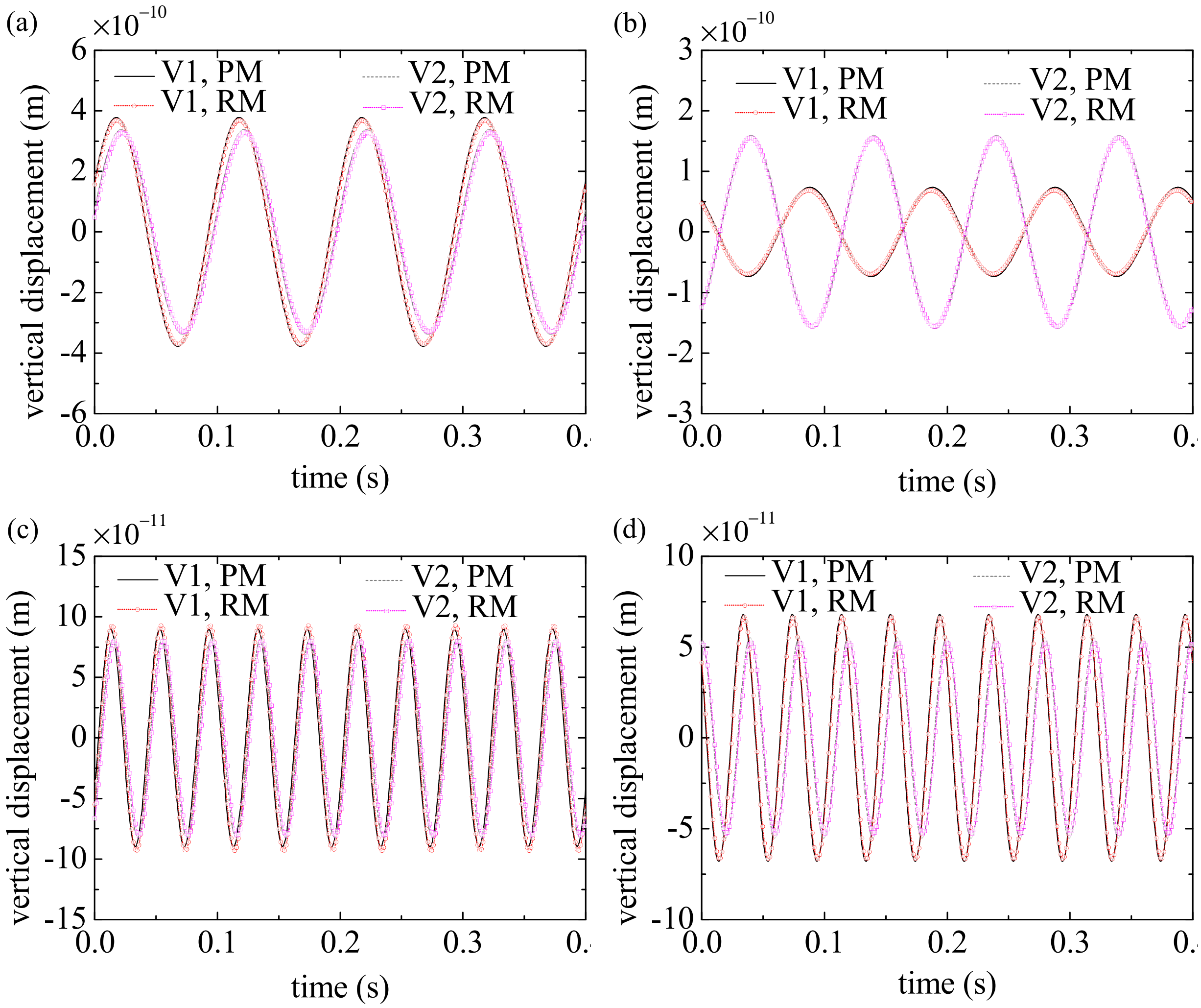

Fig. 10. Comparisons of real parts of vertical displacements of points V1 and V2 computed by the present method (PM) and the reference method (RM): (a) n=0, f_0=10 Hz; (b) n=60, f_0=10 Hz; (c) n=0, f_0=25 Hz; (d) n=60, f_0=25 Hz.

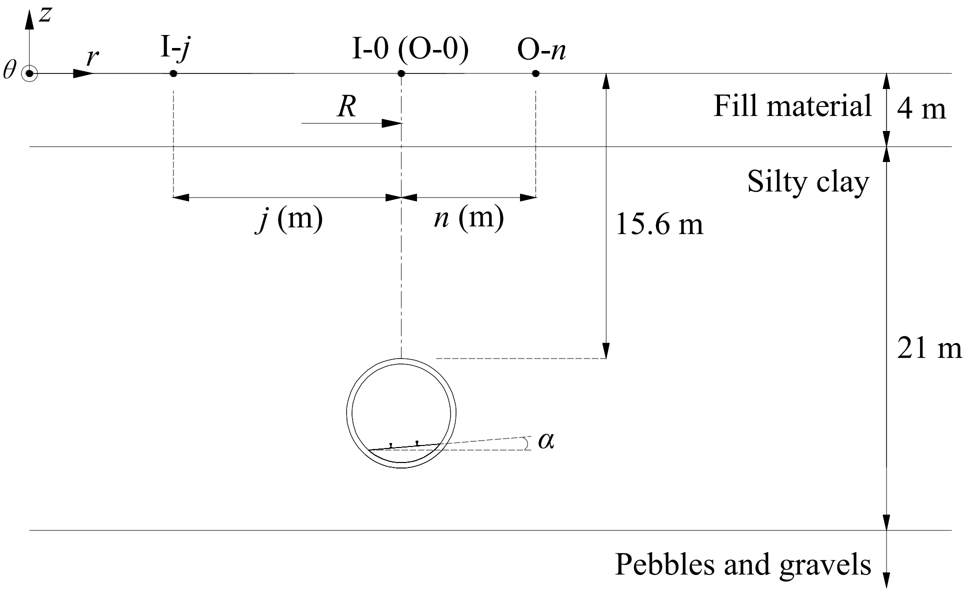

Fig. 11. Cross-sectional drawing of the track-tunnel-soil system.

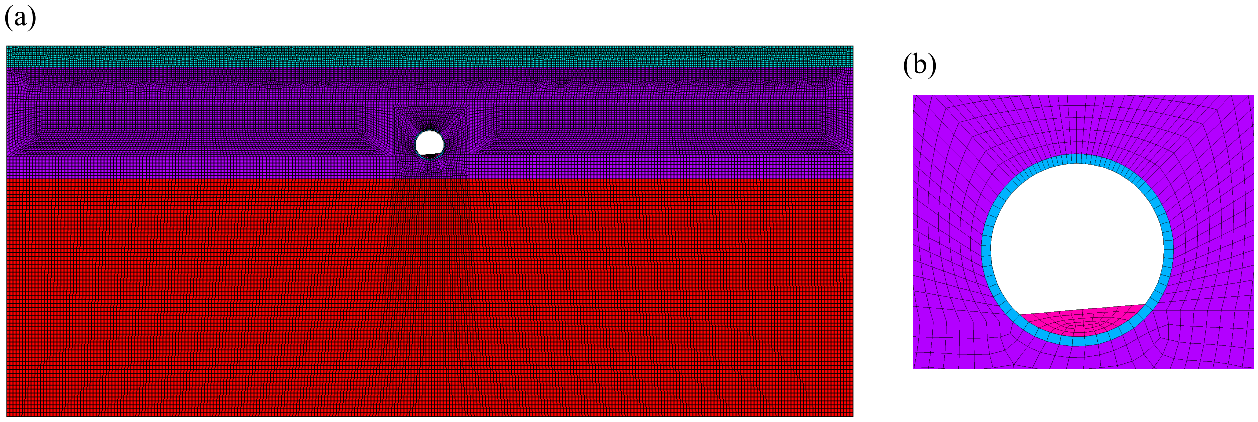

Fig. 12. Curved 2.5D FE mesh for the coupled tunnel-soil system in the curved case and that in the straight case but with a non-zero superelevation: (a) overall view of the mesh; (b) detail of the mesh.

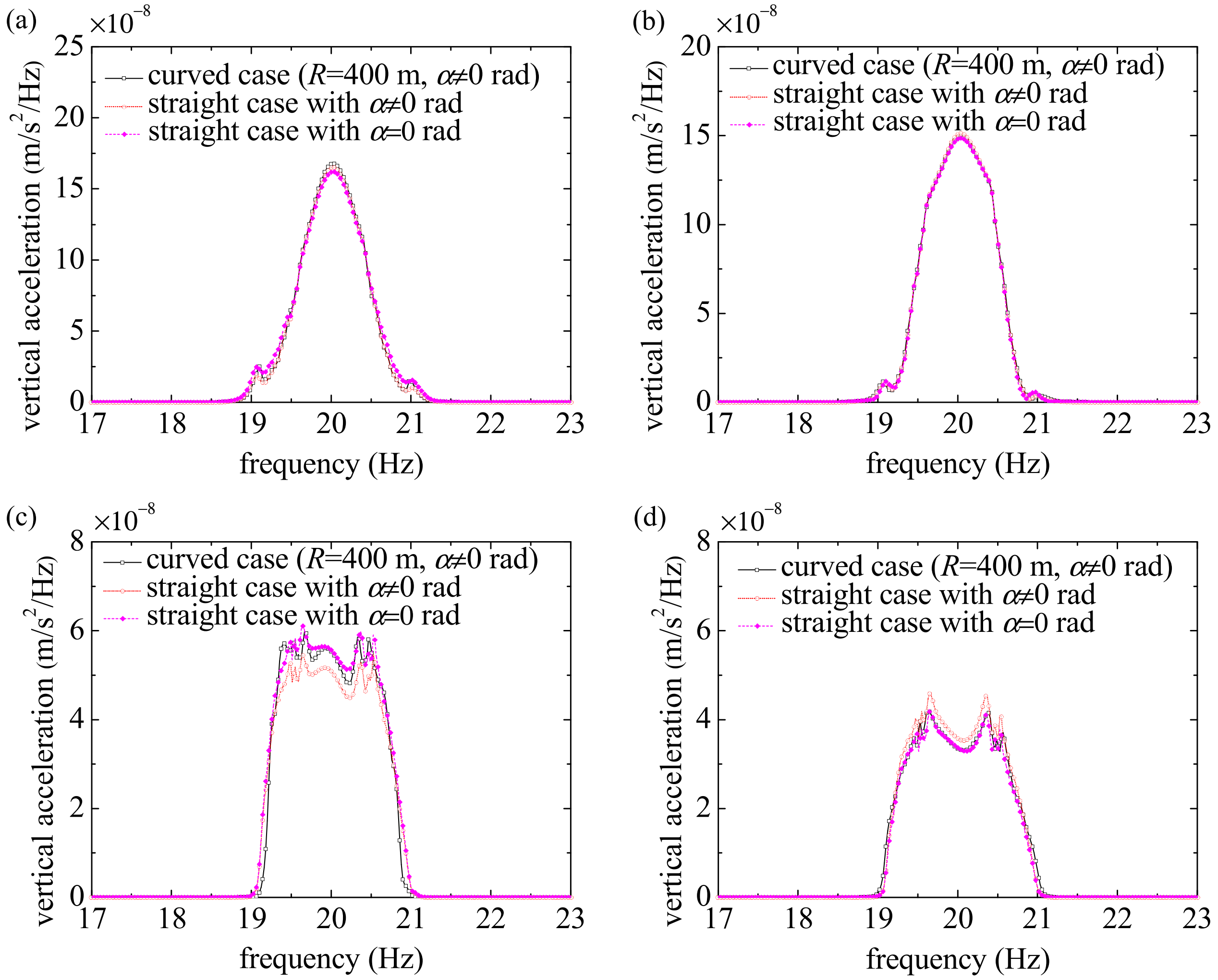

Fig. 13. Vertical acceleration spectrums of ground surface points (a) I-10, (b) O-10, (c) I-60 and (d) O-60 in the three considered structural configuration cases due to the load $P_{LZ}(t) = -\cos(2\pi f_0 t)$ with an excitation frequency of $f_0 = 20\,\text{Hz}$.

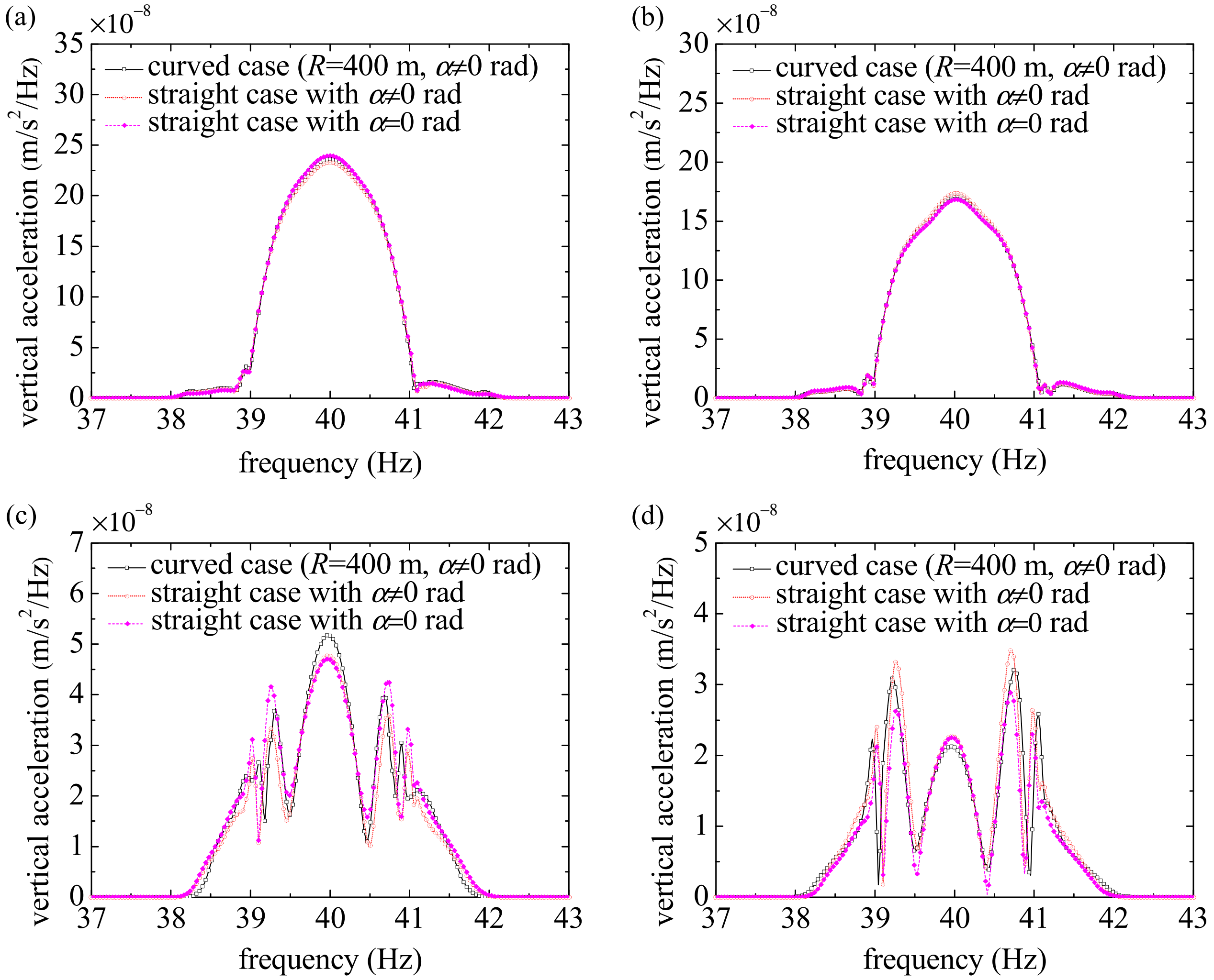

Fig. 14. Vertical acceleration spectrums of ground surface points (a) I-10, (b) O-10, (c) I-60 and (d) O-60 in the three considered structural configuration cases due to the load $P_{LZ}(t) = -\cos(2\pi f_0 t)$ with an excitation frequency of $f_0 = 40$ Hz.

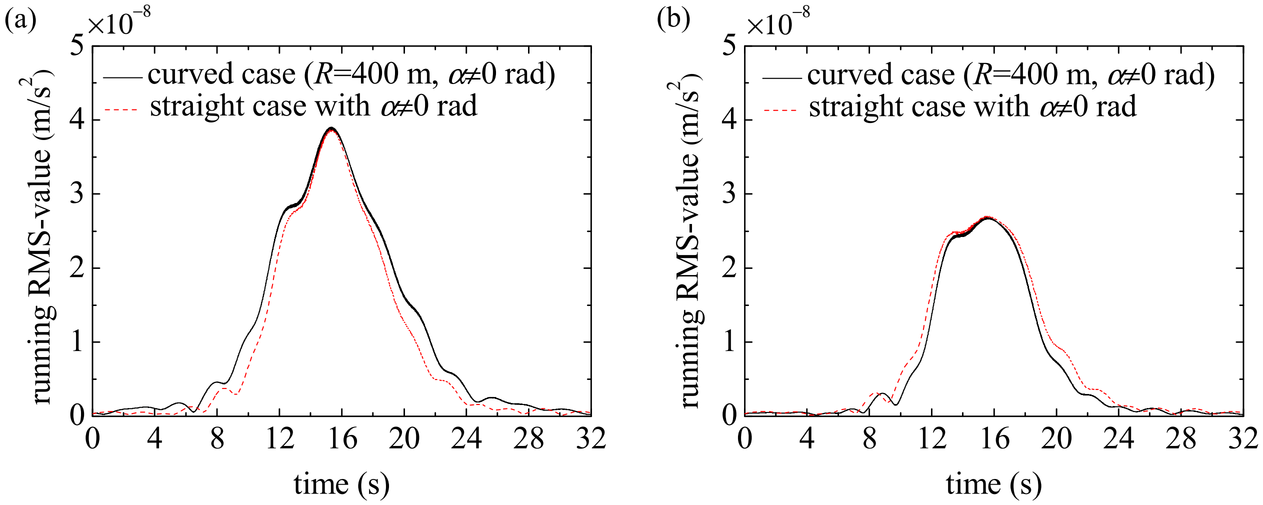

Fig. 15. Vertical acceleration running RMS-values of ground surface points (a) I-60 and (b) O-60 in the curved case and the straight case with $\alpha \neq 0$ rad due to the load $P_{LZ}(t) = -\cos(2\pi f_0 t)$ with an excitation frequency of $f_0 = 20$ Hz.

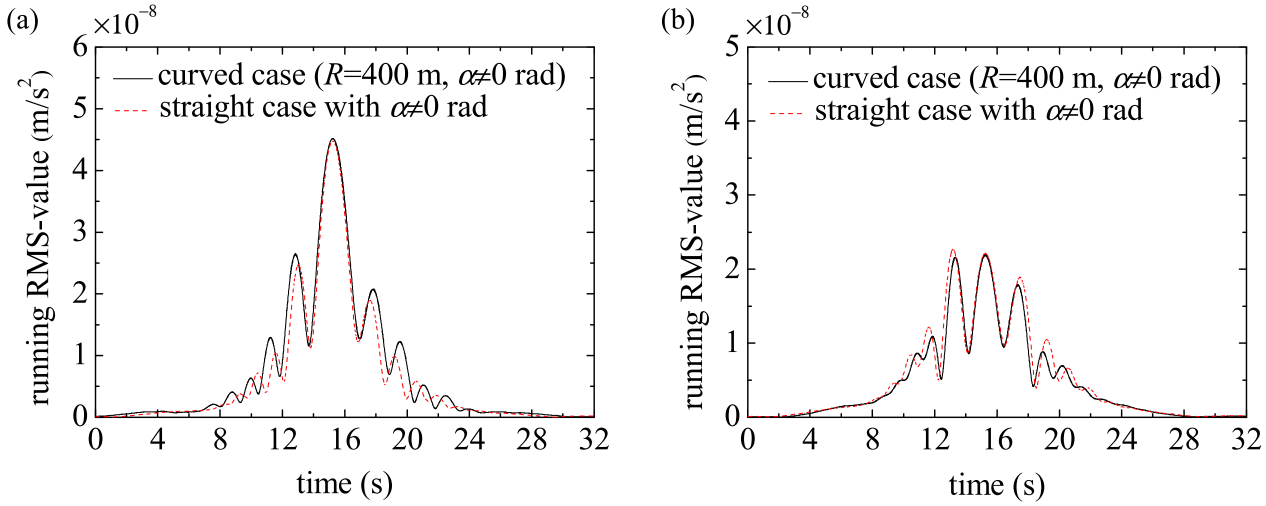

Fig. 16. Vertical acceleration running RMS-values of ground surface points (a) I-60 and (b) O-60 in the curved case and the straight case with $\alpha \neq 0$ rad due to the load $P_{LZ}(t) = -\cos(2\pi f_0 t)$ with an excitation frequency of $f_0 = 40$ Hz.

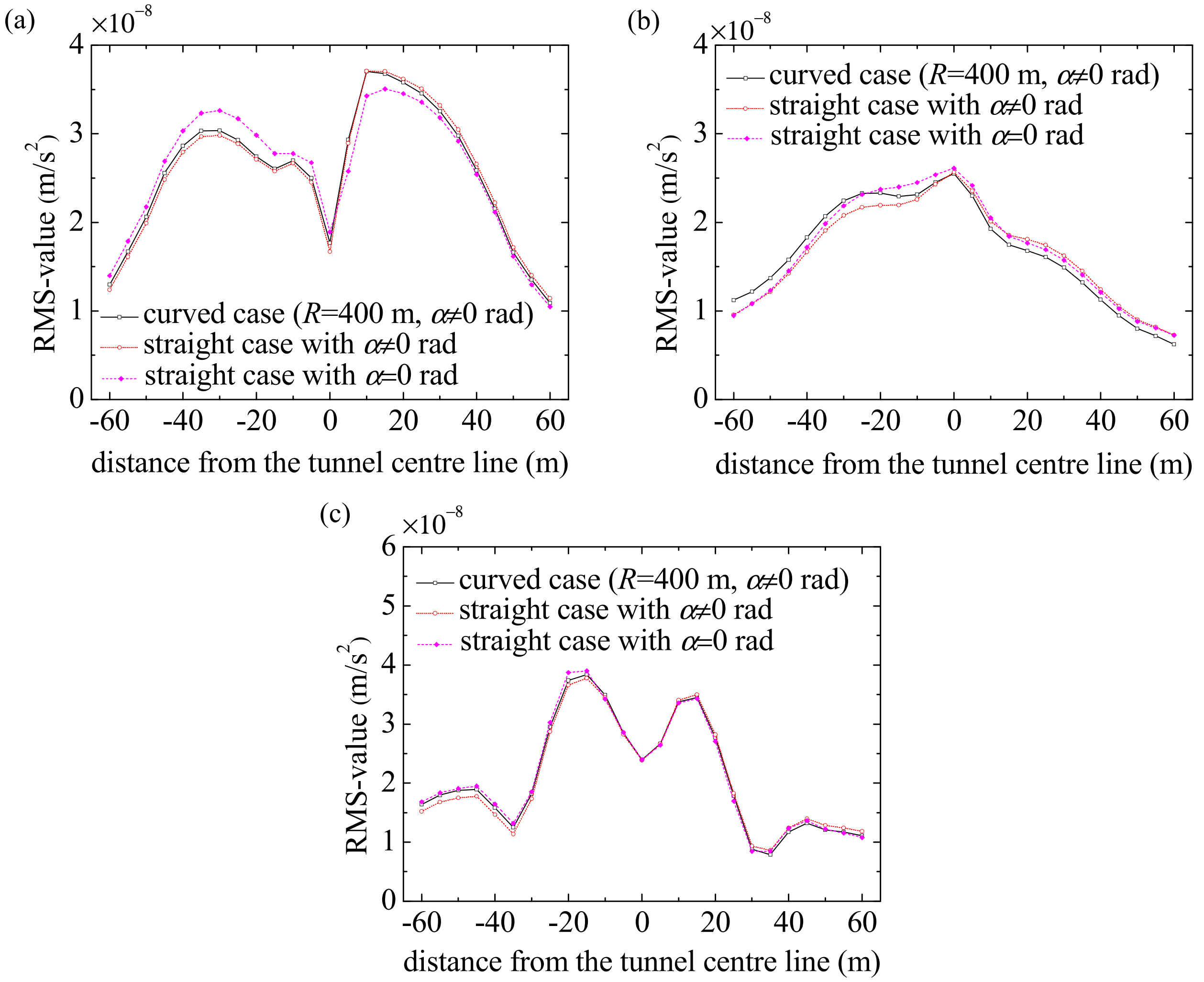

Fig. 17. RMS-values of ground surface accelerations in the (a) transverse, (b) longitudinal, and (c) vertical directions due to the load $P_{LZ}(t) = -\cos(2\pi f_0 t)$ with $f_0 = 20$ Hz versus the distance from the tunnel centre line.

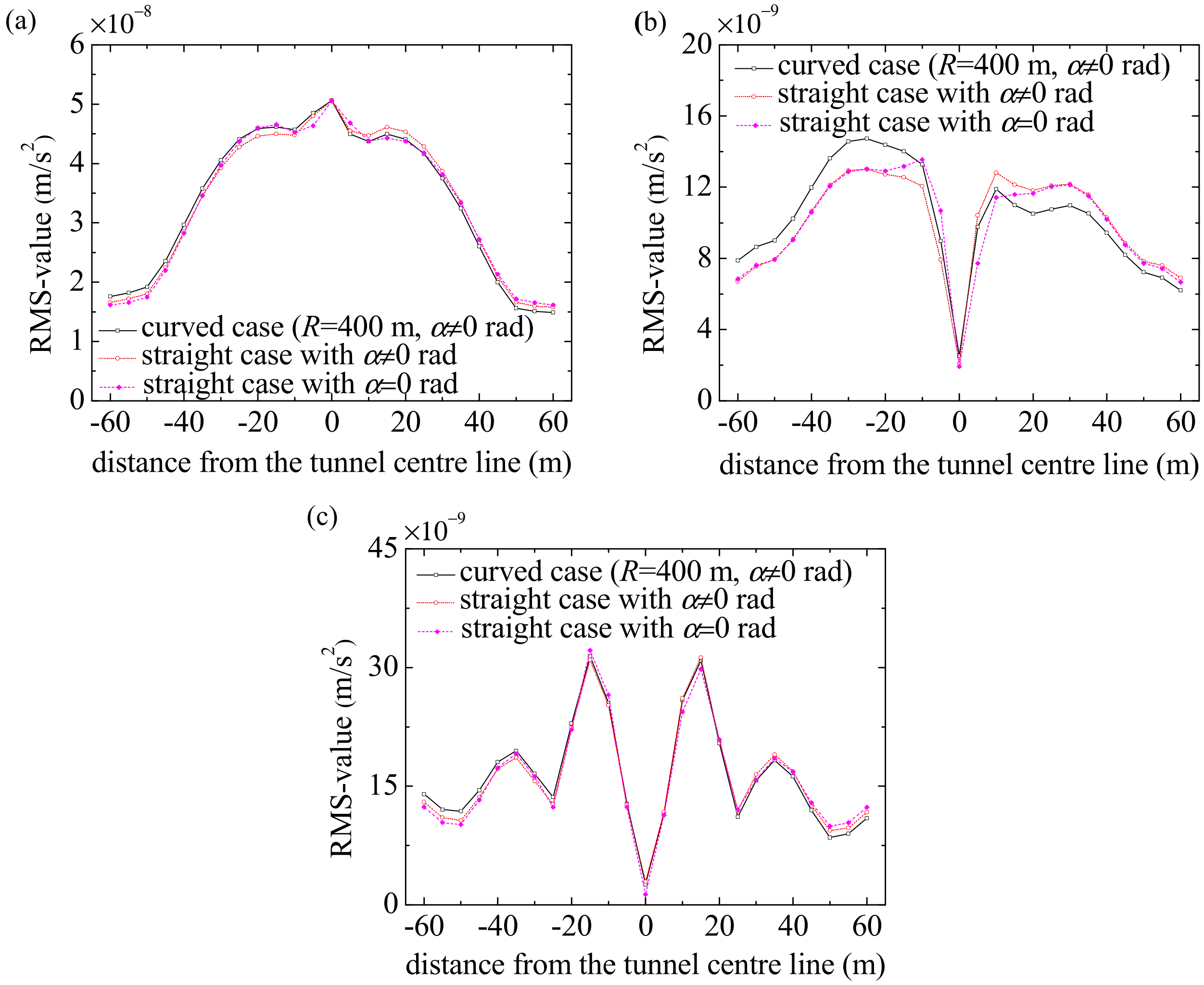

Fig. 18. RMS-values of ground surface accelerations in the (a) transverse, (b) longitudinal, and (c) vertical directions due to the load $P_{LY}(t) = -\cos(2\pi f_0 t)$ with $f_0 = 20\,\mathrm{Hz}$ versus the distance from the tunnel centre line.

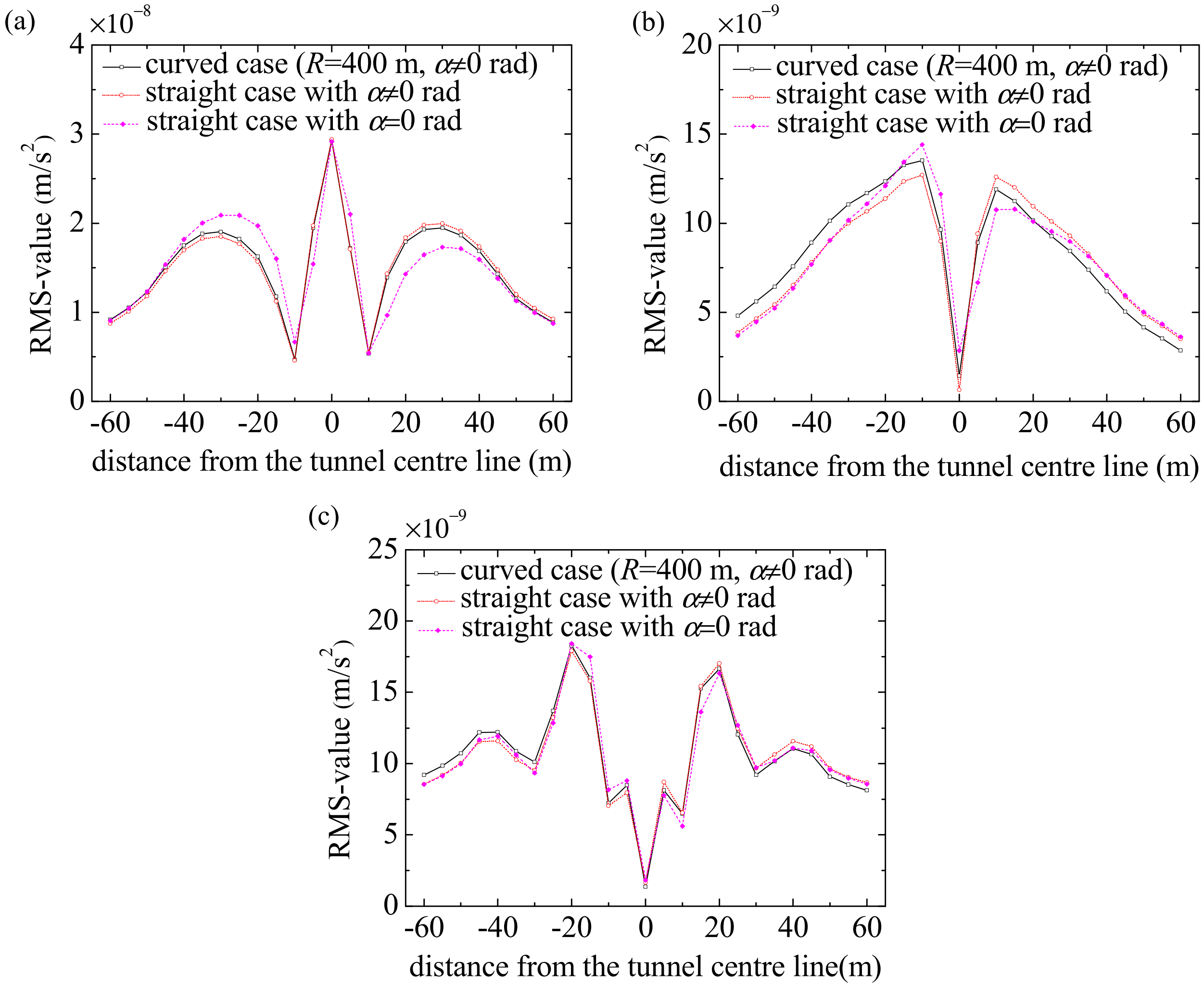

Fig. 19. RMS-values of ground surface accelerations in the (a) transverse, (b) longitudinal, and (c) vertical directions due to the load $P_{L\varphi}(t) = -\cos(2\pi f_0 t)$ with $f_0 = 20$ Hz versus the distance from the tunnel centre line.

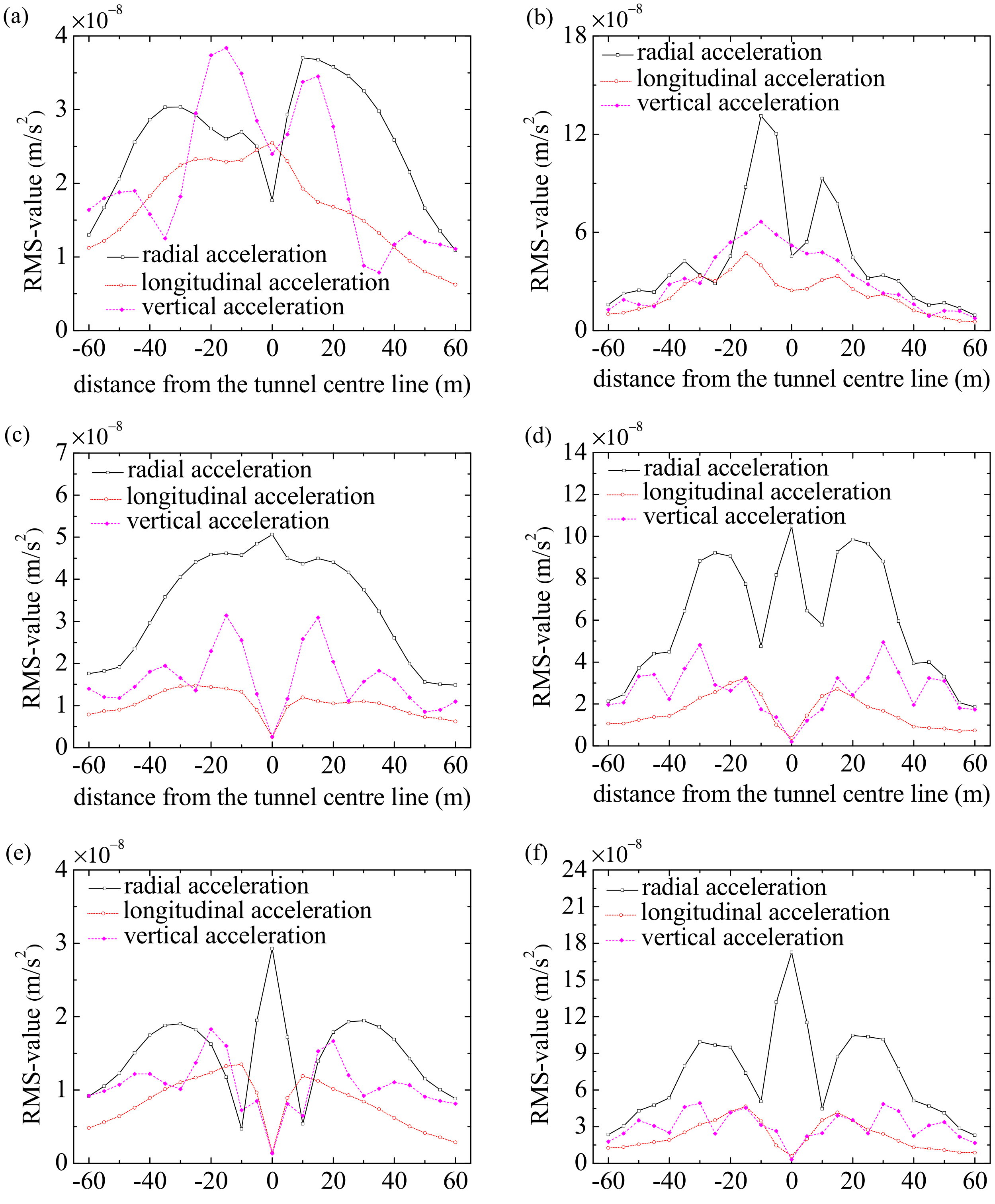

Fig. 20. Attenuation curves of the acceleration RMS-values in the curved case along the ground surface under the harmonic moving load (a) $P_{LZ}(t) = -\cos(2\pi\times 20\times t)$, (b) $P_{LZ}(t) = -\cos(2\pi\times 40\times t)$, (c) $P_{LY}(t) = -\cos(2\pi\times 20\times t)$, (d) $P_{LY}(t) = -\cos(2\pi\times 40\times t)$, (e) $P_{L\varphi}(t) = -\cos(2\pi\times 20\times t)$ and (f) $P_{L\varphi}(t) = -\cos(2\pi\times 40\times t)$.

Table 1. Physical parameters of the tunnel-soil system considered in the model validation.

medium	S-wave speed (m/s)	P-wave speed (m/s)	dynamic elastic modulus (MPa)	Poisson's ratio	density (kg/m^3)	damping ratio
soil	310.6	576.9	515	0.296	2060	0.04
tunnel base	2179.4	3559.0	28500	0.2	2500	0.02
tunnel lining	2366.4	4098.8	35000	0.25	2500	0.02

Table 2. Track parameters.

rail density ρ	7830 kg/m^3	cross-sectional area of rail A	7.745×10^{-3} m^2
Young's modulus of rail E	2.059×10^{11} Pa	shear modulus of rail G	7.919×10^{10} Pa
Damping ratio of rail ξ	0.005	torsional constant I_d	2.151×10^{-6} m^4
sectional inertia moment I_Y	3.217×10^{-5} m^4	sectional inertia moment I_Z	5.28×10^{-6} m^4
sectional inertia moment I_0	3.745×10^{-5} m^4	distance between rail centroid and bottom a	0.081 m
half width of rail bottom b	0.075 m	rail pad stiffness k_Y	4.1667×10^{7} N/m^2
rail pad damping c_Y	2.7833×10^{4} N s/m^2	rail pad stiffness k_θ	4.1667×10^{7} N/m^2
rail pad damping c_θ	2.7833×10^{4} N s/m^2	rail pad stiffness k_Z	3.3333×10^{7} N/m^2
rail pad damping c_Z	2.5×10^{4} N s/m^2		

Table 3. Physical parameters of the soil layers considered in the numerical examples.

soil layer	layer thickness (m)	S-wave speed (m/s)	P-wave speed (m/s)	dynamic elastic modulus (MPa)	Poisson’s ratio	density (kg/m^3)	damping ratio
fill material	4	180.7	351.3	138	0.32	1600	0.05
silty clay	21	310.6	576.9	515	0.296	2060	0.04
pebbles and gravels	$+\infty$	358.8	642.0	698	0.273	2130	0.03